Journal of Colloid and Interface Science 652 (2023) 1228–1239

Contents lists available at ScienceDirect

Journal of Colloid And Interface Science

journal homepage: www.elsevier.com/locate/jcis

Synthesis of germanium/germanium phosphide in-plane heterostructure with efficient photothermal and enhanced photodynamic effects in the second near-infrared biowindow

Xianwei Mo [a], Hao Huang [b,*], Caixia Sun [b,d], Zhenyu Zhang [b], Jiahong Wang [b,c], Shengyong Geng [b], Paul K. Chu [e], Xue-Feng Yu [b,c], Wenxin Liu [a,*]

[a] Zhanjiang Institute of Clinical Medicine, Zhanjiang Central Hospital, Guangdong Medical University, Zhanjiang 524045, China
[b] Shenzhen Key Laboratory of Micro/Nano Biosensing, Shenzhen Institute of Advanced Technology, Chinese Academy of Sciences, Shenzhen 518055, China
[c] Hubei Three Gorges Laboratory, Yichang, Hubei 443007, China
[d] The First Clinical Medical School, Guangdong Medical University, Zhanjiang 524023, China
[e] Department of Physics, Department of Materials Science and Engineering, and Department of Biomedical Engineering, City University of Hong Kong, Tat Chee Avenue, Kowloon, Hong Kong, China

GRAPHICAL ABSTRACT

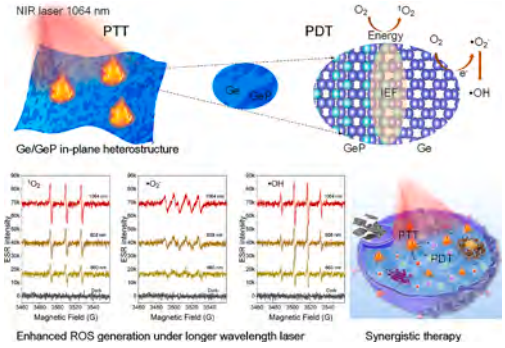

ARTICLE INFO

Keywords:
Second near-infrared biowindow
Germanium
In-plane heterostructure
Photothermal therapy
Photodynamic therapy

ABSTRACT

Inspired by the bifunctional phototherapy agents (PTAs), constructing compact PTAs with efficient photothermal therapy (PTT) and photodynamic therapy (PDT) effects in the near-infrared (NIR-II) biowindow is crucial for high therapeutic efficacy. Herein, none-layered germanium (Ge) is transformed to layered Ge/germanium phosphide (Ge/GeP) structure, and a novel two-dimensional sheet-like compact S-scheme Ge/GeP in-plane heterostructure with a large extinction coefficient of 15.66 L/g cm^{-1} at 1,064 nm is designed and demonstrated. In addition to the outstanding photothermal effects, biocompatibility and degradability, type I and type II PDT effects are activated by a single laser. Furthermore, enhanced reactive oxygen species generation under longer wavelength NIR laser irradiation is achieved, and production of singlet oxygen and superoxide radical upon 1,064 nm laser irradiation is more than double that under 660 nm laser irradiation. The S-scheme charge transfer mechanism between Ge and GeP, is demonstrated by photo-irradiated Kelvin probe force microscopy

* Corresponding authors.
E-mail addresses: hao.huang@siat.ac.cn (H. Huang), wenxin_liu@gdmu.edu.cn (W. Liu).

https://doi.org/10.1016/j.jcis.2023.08.137
Received 12 July 2023; Received in revised form 16 August 2023; Accepted 21 August 2023
Available online 23 August 2023

and electron spin resonance analysis. Thus, the obtained S-scheme Ge/GeP in-plane heterostructure shows synergistic therapeutic effects of PTT/PDT both *in vitro* and *in vivo* in the NIR-II biowindow and the novel nanoplatform with excellent properties has large clinical potential.

1. Introduction

Phototherapy, an emerging light-enabled cancer treatment boasting minimal invasiveness, precise spatial selectivity, simple operation, and strong anti-tumor ability has large clinical potential [1]. Particularly, phototherapy in the second near-infrared (NIR-II, 1000–1700 nm) biowindow endows higher permissible exposure and greater penetration depth without skin damage compared with the first NIR (NIR-I, 700–950 nm) biowindow [2–5]. However, single-mode phototherapy such as photothermal therapy (PTT) that utilizes light-induced thermal conversion to kill cancer cells and photodynamic therapy (PDT) that generates reactive oxygen species (ROS) to induce apoptosis of cancer cells under light irradiation is still plagued by the limited therapeutic efficacy resulting from the suboptimal photo-heat conversion efficiency and photodynamic types [1,5,6]. In type I PDT, the phototherapy agents (PTAs) serve as the photosensitizers and utilize e^-/H^+ to generate active radicals such as the superoxide radical ($\bullet O_2^-$) or hydroxyl radical (•OH) and are thus oxygen tolerant [7,8]. In the type II process, the triplet photosensitizers can transfer the energy to the surrounding O_2 to generate singlet oxygen ($^1O_2$) thereby depending on the amount of O_2 [9]. However, most of the PTAs rely on the type II process, and the therapeutic efficacy is limited in the hypoxic tumor environment. The combination of type I and type II PDT may be a good choice [9–11]. On the other hand, the synergistic effects of PTT and PDT can compensate each other, that is, PTT improving the O_2 supply and PDT inhibiting the hot shock proteins [12]. The combination of PTT and PDT in the NIR-II biowindow has become a popular research topic [2,3]. Unfortunately, bifunctional PTAs with both PTT and PDT effects in the NIR-II biowindow are still scare, especially ones showing integrated type I and type II PDT effects [3]. Moreover, most of the reported bifunctional PTAs combine two or several functional materials, which involve complicated structures, tedious synthesis process, and potential dissociation [2,6,13]. Hence, it is crucial to design a single and compact NIR-II bifunctional PTA with high therapeutic efficacy.

Recently, two-dimensional (2D) layered materials have garnered tremendous interests in electronics, quantum devices, and biomedicine [5,6,14,15]. In particular, materials with excellent photoelectronic and photocatalytic properties and outstanding biocompatibility have been developed as potential anti-tumor agents for PTT, PDT, drug vehicles and imaging, for instance, 2D phosphorene, borophene and germanene based materials [6,16–18]. By loading drugs or constructing heterostructures, multimodal combination therapy triggered by 2D materials such as PTT with PDT, PTT with chemodynamic therapy can be achieved [1,6,19,20]. However, most of these experiments have focused on the NIR-I biowindow and need dual-laser irradiation [18,20–24]. Both phosphorus and germanium are essential elements in the human body [16,18]. As the second most common element in our body, phosphorus (P) accounts for 1% of the body weight and germanium (Ge) is a trace element associated with the human health and immunoregulation [17]. P-based and Ge-based materials have great biocompatibility and potential medical value. Compared to 2D phosphorene-based anti-tumor agents, 2D Ge-based biomaterials have been scarcely explored aside from several works in the NIR-I biowindow, for example, Ge quantum dots for PTT [18], drug-loaded Ge@hydrogel for tumor surgical adjuvant therapy [20], and drug modified germanium phosphide (GeP) hybrids for multimodal cancer theranostics [24]. The biomedical applications of 2D Ge-based materials in the NIR-II biowindow have yet to be explored. Moreover, unlike Graphene or other 2D layered materials, Ge has no layered bulk counterparts which also imposes restrictions on the preparation of Ge-based thin sheets and its applications.

Herein, a novel strategy is proposed to transform bulk Ge crystal to layered structure by partially transforming Ge to layered GeP *in situ*. A 2D sheet-like and compact S-scheme Ge/GeP in-plane heterostructure is demonstrated to be an efficient PTA to deliver excellent PTT and type I, type II PDT effects simultaneously in the NIR-II biowindow when activated by a single 1,064 nm laser in tumor therapy (Scheme 1). The chemical vapour transport (CVT) method was used to synthesize the bulk Ge/GeP crystal *in situ* and a top-down approach involving grinding and sonication is implemented in the synthesis of Ge/GeP nanosheets (NSs). The Ge/GeP NSs show strong absorption spanning the visible range to the NIR-II biowindow with a large extinction coefficient at 1,064 nm. In addition to the outstanding photothermal effects, biocompatibility, and degradability, both type I and type II PDT effects are achieved by the energy/electron transfer process under single NIR laser irradiation due to the unique in-plane Ge/GeP heterostructure. Moreover, to the best of our knowledge, enhanced ROS generation upon longer NIR wavelength laser irradiation is observed for the first time report on Ge-based materials. The S-scheme charge transfer mechanism between Ge and GeP is verified by photo-irradiated Kelvin probe force microscopy (KPFM) and electron spin resonance (ESR) analysis. The formation of such S-scheme Ge/GeP heterostructure endows the PTA with boosted charge separation. As a result, the Ge/GeP NSs show excellent phototherapy effects both *in vitro* and *in vivo* in the NIR-II biowindow with negligible toxicity to normal cells. This novel therapeutic nanoplatform has large clinical potential and our results provide insights into the design of efficient PTAs for precision medicine.

2. Experimental section

2.1. Materials

The Ge (≥99.999%), red P crystals (≥99.99%), 2,7-dichloro-dihydro-fluorescein diacetate (DCFH-DA, ≥97%) and *N*-methyl-2-

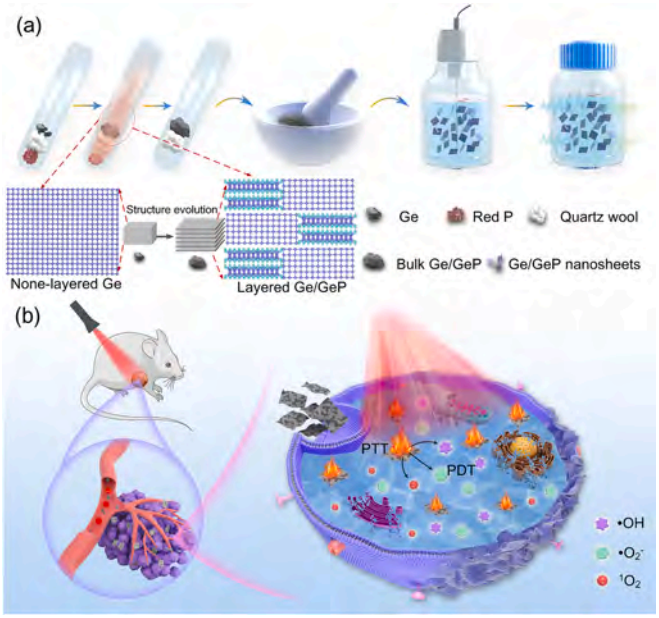

Scheme 1. A schematic of the synthesis of Ge/GeP NSs for synergistic phototherapy. (a) Schematic illustration of the synthesis of Ge/GeP NSs and (b) Application to NIR-II synergistic PTT-type I, type II PDT phototherapy.

pyrrolidone (NMP, ≥99.5%) were obtained from Aladdin Co. Ltd (Shanghai, China) and Dulbecco's modified Eagle medium (DMEM), Roswell Park Memorial Institute-1640 (RPMI-1640) medium and fetal bovine serum (FBS) and phosphate buffer saline (PBS, pH 7.4) were purchased from ThermoFisher Biochemical Products Co. Ltd. (Beijing, China). The Calcein-AM/PI cell viability/cytotoxicity assay kit and Annexin V-FITC apoptosis detection assay kit were obtained from Beyotime Biotechnology Co. Ltd (Shanghai, China). All the chemicals were used without further purification and ultrapure water (18.25 MΩ•cm, 25 °C) was used to prepare the solutions.

2.2. Synthesis of Ge/GeP NSs

Typically, 0.6 g Ge and 0.43 g red P were placed and separated by a piece of asbestos inside an evacuated and sealed quartz tube. The tube was placed in a two-zone tube furnace. The sample side and other side were heated slowly to 850 °C and 800 °C in 200 min and kept for 10 h before cooling to room temperature naturally. The product was purified to remove excess P, put in the quartz tube, evacuated, and sealed. The sample side was heated slowly to 500 °C and the other side to 450 °C in 60 min and kept for 8 h. Finally, the tube cooled naturally to room temperature.

To obtain Ge/GeP NSs, a simple liquid exfoliation method was used. 100 mg of bulk Ge/GeP and a small amount of the NMP solvent were ground for 3–5 min in an agate mortar and the Ge/GeP/NMP slurry was transferred to a 250 mL glass bottle. The dispersion with a volume of 90 mL was sonicated with a sonic tip for 10 h at the power of 600 W at a low temperature (6–10 °C) and the ultrasound probe was operated for 2 s with an interval of 4 s, followed by sonication in an ultrasonic bath for 4 h using the power of 300 W. After the ultrasonic treatment, the Ge/GeP NSs/NMP supernatant was obtained by centrifugation at a speed of 7,000 rpm for 15 min. The Ge/GeP NSs were obtained at a higher centrifugation speed of 13000 rpm for 15 min and then washed repeatedly with water to remove excess NMP.

2.3. Characterization

Scanning electron microscopy (SEM) was conducted on the Zeiss Supra 55 field-emission microscope (Carl Zeiss, Germany). Transmission electron microscopy (TEM) and high-resolution TEM (HRTEM) were carried out on the Talos F200X transmission electron microscope (FEI, USA) at an acceleration voltage of 200 kV. The X-ray diffraction (XRD) patterns were recorded on the SmartLab X-ray diffractometer with Cu K_α radiation (40 kV, 30 mA) (Rigaku, Japan). Atomic force microscopy (AFM) was performed on the Cypher S AFM (Asylum Research, USA) and Raman scattering was carried out on the high-resolution confocal Raman microscope with the 633 nm laser as the excitation source (Horiba Jobin-Yvon Lab Ram HR VIS, Horiba, France). The concentrations of the Ge/GeP NSs were determined by inductively-coupled plasma atomic emission spectroscopy (ICP-OES, Agilent 730, Agilent Technologies). X-ray photoelectron spectroscopy (XPS) was conducted on the Thermo Fisher ESCALAB 250Xi (Thermofisher, USA) and the absorption spectra were acquired from the TU-1810 spectrophotometer (Purkinje General Instrument Co. Ltd. Beijing, China) using QS-grade quartz cuvettes at room temperature. The solid-state diffuse reflectance absorption spectrum was acquired on the UV–vis spectrophotometer (UV-3600, Shimadzu, Japan).

2.4. Photothermal properties of Ge/GeP NSs

The photothermal properties of the Ge/GeP NSs were determined using a custom instrument with a fiber-coupled continuous semiconductor diode 1064 nm (NIR II) laser (LWIRL 1064–3 W, Beijing Laserwave Optoelectronics Technology Co. Ltd. China) as the light source. The suspensions (1 mL) with different concentrations of dispersed Ge/GeP NSs were put in 1 cm path-length quartz cuvettes and irradiated with the 1,064 nm laser. The temperature variation was recorded by an infrared thermal imaging camera (Fluke Ti27, USA).

2.5. Extinction coefficient

To evaluate the NIR absorption capability of the Ge/GeP NSs, the extinction coefficient ε(λ) of the Ge/GeP NSs is determined according to the Lambert-Beer law: A (λ) = εLC, where A is the absorbance at the wavelength λ, L is the path length (1 cm), and C is the concentration of the Ge/GeP NSs (in g/L). The ε is calculated by plotting the slope (in L/g cm^{-1}) of each linear fit against wavelength.

2.6. Photothermal conversion efficiency

The photothermal conversion efficiency (η) of the Ge/GeP NSs is calculated by Eq. (1):

$$\eta = \frac{hS(T_{Max} - T_{Surr}) - Q_{Dis}}{I(1 - 10^{-A_{1064}})} \quad (1)$$

where h is heat transfer coefficient, S is the surface area of the cuvette, T_{max} and T_{Surr} represent the equilibrium and ambient temperature respectively, Q_{Dis} is the heat dissipated from light absorbed by the cuvette itself, I is the NIR II laser power density, and A_{1064} is the absorbance of the Ge/GeP NSs (100 μg mL^{-1}) at 1,064 nm. In this equation, hS is determined according to Eq. (2):

$$hS = \frac{mC}{\tau} \quad (2)$$

where m and C are the mass and heat capacity of the solvent, pure water, m is 1.0 g, and C is 4.2 J g^{-1}. To determine τ, a dimensionless driving force temperature θ is introduced as defined by Eq. (3):

$$\theta = \frac{T - T_{Surr}}{T_{Max} - T_{Surr}} \quad (3)$$

The time constant of heat transfer τ is calculated by Eq (4) based on the cooling duration:

$$t = \tau(-\ln\theta) \quad (4)$$

where T is the real-time temperature of the sample when the laser is turned off, t represents time. Therefore, hS is derived and the η of the Ge/GeP NSs at 1,064 nm is determined.

2.7. Electron spin resonance (ESR)

ESR was carried out to identify the type of ROS using 2,2,6,6-tetramethylpiperidine (TEMP) as the $^1O_2$ indicator and 5-*tert*-butoxycarbonyl-5-methyl-1-pyrroline-*N*-oxide (BMPO) as the $•O_2^-$ and $•OH^-$ indicator. The ESR spectra were collected from mixtures including 200 μL of Ge/GeP NSs (1 mg mL^{-1}) in water and 200 μL of TEMP or BMPO (100 mM) upon 1,064 nm light (1.0 W cm^{-2}) irradiation for 5 min. The solution was put in the ESR cavity and the ESR data were collected on the Bruker Model A300-10/12 spectrometer (Billerica, MA, USA) at 298 K. The testing parameters were as follows: frequency = 9.85 GHz, microwave power = 19.32 mW, sweeping time = 40.96 s, sweeping width = 100 G, and modulation frequency = 100 kHz. The control group without laser exposure was studied for comparison.

2.8. In vitro cytotoxicity

The Hela (cervical tumor), MCF-7 (breast tumor), and QSG-7701 (normal liver) cells were purchased from China Type Culture Collection (CTCC) obtained from the American Type Culture Collection (ATCC). The cells were cultured in a humidified 5% CO_2 atmosphere with DMEM or RMPI-1640 (for QSG-7701) supplemented with 10% FBS at 37 °C. The *in vitro* cytotoxicity of Ge/GeP NSs was evaluated by the

flow cytometry-based Annexin V-FITC/propidium iodide assay. In brief, the cells were seeded on 48-well plates (10^4 cells/well) and cultured overnight. The medium was replaced with 200 μL of the medium containing 100 μg mL^{-1} of Ge/GeP NSs and incubated for 24 h. Afterwards, the cells were collected, and stained with Annexin V-FITC and PI according to the manufacturer's instruction, followed by flow cytometry performed on the Beckman CytoFLEX flow cytometer.

2.9. Cellular uptake of Ge/GeP NSs

The Hela or MCF-7 cells were seeded on a 24-well culture plate with climbing glass (2×10^4 cells/well) and cultured overnight to form a mono-layer. The cells were treated with 0.5 mL of the medium containing Ge/GeP NSs with a concentration of 25 μg mL^{-1} at 37 °C for 4 h. After removing the culture medium, the cells were rinsed three times with PBS. The glass side was transferred onto a glass slide and the cells were observed and imaged *via* a microscope (BX53M, Olympus). The Ge/GeP NSs inside the cell were analyzed by Raman scattering.

2.10. Intracellular ROS

Intracellular generation of ROS was determined by DCFH-DA as a fluorescent probe. Briefly, the Hela and MCF-7 cells were incubated on a 48-well plate and cultured for 24 h. The cells were divided randomly into four groups and received different treatments: (1) Control group (untreated cells), (2) laser irradiation group, (3) Ge/GeP NSs (100 μg mL^{-1}, 0.2 mL) treated group, (4) Ge/GeP NSs (100 μg mL^{-1}, 0.2 mL) + laser irradiation treated group. The Ge/GeP NSs treated group and Ge/GeP NSs + laser irradiation treated group were incubated with the medium containing 100 μg mL^{-1} of Ge/GeP NSs for 4 h, and then rinsed with PBS twice. The DCFH-DA (0.2 mL, 20 μM in serum-free culture medium) was added to each well and incubated at 37 °C under 5% CO_2 for 30 min in the dark. The laser irradiation group and Ge/GeP NSs solution + laser irradiation treated group were irradiated with a 1,064 nm laser (1.0 W cm^{-2}) for different time. After the treatment, the cells were washed twice with PBS and examined under a fluorescence microscope (IX71, Olympus).

2.11. In vitro phototherapy

The cellular viability was evaluated to determine the therapeutic efficiency *in vitro*. The Hela and MCF-7 cells were treated with the Ge/GeP NSs solutions (0, 25, 50 and 100 μg mL^{-1}), incubated at 37 °C for 4 h, and exposed to the 1,064 nm laser with the power of 0.5, 1.0 or 1.5 W cm^{-2} for different time. The laser spot was adjusted to fully cover the area of each well. After incubation for 12 h at 37 °C, flow cytometry was employed to examine the cellular viability according to the manufacturer's protocol. The cells were also rinsed with PBS and stained with Calcein-AM/PI dyes to reveal the therapeutic efficiency of Ge/GeP NSs *in vitro*.

2.12. Calcein acetoxymethyl ester (calcein AM) and propidium iodide (PI) dual-staining

The Hela cells and MCF-7 cells were seeded on a 48-well plate and cultured for 12 h. The cells were incubated with the complete medium containing Ge/GeP NSs with a predetermined concentration for 4 h. The cells were then irradiated with a 1,064 nm laser (1.0 W cm^{-2}) and incubated for 12 h in a 5% CO_2, 95% air humidified incubator at 37 °C. Afterwards, the treated cells were washed and co-stained with Calcein AM/PI according to the manufacturer's protocol and then examined under an inverted fluorescence microscope (IX71, Olympus). The live cells were stained with Calcein AM to exhibit green fluorescence and the dead cells were stained with PI to show red fluorescence.

2.13. Flow cytometry

The Hela cells and MCF-7 cells were seeded on a 48-well plate in the DMEM medium supplemented with 10% FBS and incubated in a 37 °C humidified incubator (5% CO_2) for 24 h. The cells were exposed to 100 μg mL^{-1} of Ge/GeP NSs for 4 h and irradiated with a 1,064 nm laser (1.0 W cm^{-2}) for different time. After irradiation, the cells were incubated for 12 h in a 5% CO_2, 95% air humidified incubator at 37 °C. Subsequently, according to the manufacturer's instruction for the Annexin V-FITC apoptosis detection assay kit, the cells were collected by centrifugation and detected by flow cytometry (Beckman CytoFLEX). The fluorescence intensity was quantified by the flowJo 10.6.2 software.

2.14. In vivo anticancer studies

All the animal experiments were conducted in accordance with the guidelines of by Wuhan Servicebio Technology Co., Ltd., China and the ethical approval protocol number was Servicebio Animal Welfare NO.2022011. The BALB/c nude mice (female, 5–6 weeks old) were purchased from Beijing Vital River Laboratory Animal Technology Co., Ltd. 1×10^7 MCF-7 cells in 100 μL PBS were subcutaneously injected into the left foreleg armpit of each mouse and the tumor size was measured periodically by a slide caliper. When the tumor volume approached ~ 250 mm^3, the mice were used for further experiments.

The tumor-bearing BALB/c nude mice were randomized into four groups (n = 5 for each group): (1) Control group, (2) Ge/GeP NSs treated group, (3) NIR treated group, (4) Ge/GeP NSs + NIR treated group. For the control group and NIR treated group, aliquots (100 μL) of PBS were administered by intratumoral injection, while the Ge/GeP NSs treated group and Ge/GeP NSs + NIR treated group of mice were intratumorally injected with 100 μL of Ge/GeP NSs (300 μg mL^{-1}) in PBS. At 2 h post-injection, the mice were anaesthetized and the entire region of the tumor was exposed to the 1,064 nm laser (1.0 W cm^{-2}) for 10 min. At the same time, an infrared thermal imaging camera (Ti27, Fluke, USA) was employed to monitor the temperature of the tumors and acquire the infrared thermographic maps. After laser irradiation, the tumor size was measured by a caliper every other day according to the formula: volume (V) = (tumor length) × (tumor width)^2/2, and no mice died during the process. The same person performed all the tumor measurements in this study. The relative tumor volume was calculated as V/V_0 with V_0 being the initial tumor volume at the beginning of the treatment. On the 14th day, the mice were euthanized and the major organs (heart, liver, spleen, lung, and kidney) and tumor tissues were extracted and fixed in 10% formalin. Blood was collected for hematological and blood biochemical analysis. The major organs and tumor issues were sectioned into slices and stained with hematoxylin and eosin (H&E), transferase dUTP nick end labeling (TUNEL) and Ki-67 in the histological analysis.

2.15. Statistical analysis

All the results were expressed as mean ± standard deviation (SD) and comparison was based on the two-tailed Student's *t* test with (*) $P < 0.05$, (**) $P < 0.01$, and (***) $P < 0.001$.

3. Results and discussion

3.1. Synthesis and characterization of the Ge/GeP in-plane heterostructure

The bulk Ge/GeP crystal was synthesized by a modified CVT method (Scheme 1a) [25]. The large Ge crystal was separated with the P source and the P vapor was transported to the Ge side at an elevated temperature to form the Ge/GeP structure *in situ*. During this process, the Ge-Ge bond is broken by P vapor and forming layered GeP which causes the expansion. Finally, an intercalation-like effect makes the covalent bond force between Ge atoms become van der Waals force (Scheme 1a). As

expected, the smooth Ge crystal has become a layered structure and the volume is enlarged twice (Fig. 1a, b). The surface of the bulk Ge/GeP shows a porous network connected by small crystals (Fig. S1), and the XRD pattern of the Ge/GeP powder can be indexed to the cubic Ge (JCPDS 04–0545) and layered GeP (JCPDS 44–1125), indicating the coexistence of Ge and GeP (Fig. S2).

The intermediate product is investigated (Fig. S3) and it is found that there exists an etching and *in-situ* transformation process which may contribute to the formation of the unique Ge/GeP structure. Due to the layered structure, the Ge/GeP NSs can be easily exfoliated by simple grinding and sonication. As shown in Fig. 1c, d, the Ge/GeP NSs exhibit a typical 2D sheet-like morphology with no small particles on the surfaces. The thickness ranges from 15 to 32 nm and the average lateral size is 153 ± 39 nm (Fig. S4a, b). Also, the hydrated particle size is measured by using a laser particle size analyzer. A larger average size of about 170 nm can be found, which is due to the formation of hydrated layer on Ge/GeP NSs (Fig. S4c). The HR-TEM images of one Ge/GeP NS show a polycrystalline nature and the lattice distances of 3.25 Å, 2.01 Å, 1.42 Å and 6.35 Å can be assigned to the (111), (220), (400) planes of Ge as well as (001) plane of GeP (Fig. 1e, f). The overlapping diffraction rings in the selected-area electron diffraction (SAED) pattern (Fig. 1g) confirm the polycrystalline nature [26], which can be assigned to the (111) plane of Ge, or (−311) plane of GeP, (220) plane of Ge or (−913) plane of GeP, and (311) plane of Ge or (-11 14) plane of GeP, respectively. The 2D layered structure with a polycrystalline surface nature suggests the in-plane heterostructure of Ge/GeP NS. The high angle annular dark field (HAADF) image and elemental maps acquired from one Ge/GeP NS show uniformly distributed Ge and P without obvious contrast difference at the same thickness area (Fig. 1h-j), indicating that the Ge components are ultrasmall and without significant aggregation during formation of the Ge/GeP in-plane heterostructure (Fig. 1k).

The Ge/GeP NSs dispersed in NMP have a yellow–brown color and the powder exhibits broad vis-NIR absorption from 450 to 1,800 nm with peaks at 1,195 (1.03 eV), 1,440 (0.86 eV), and 1,717 nm (0.72 eV) (Fig. 2a) in good agreement with reported optical properties of Ge nanocrystals with obvious quantum confinement effects that arise a size-dependent band gap [27–29]. The crystal structure of the Ge/GeP NSs is determined as shown in Fig. 2b. The XRD pattern reveals overlapping crystalline domains of Ge and GeP. The strong (001) peak at 13.87° shows the preferred orientation of layered GeP. Also, the XRD peaks at 20.88°, 23.98°, 29.70°, 30.38°, 33.11°, 34.16° and 50.13° are from the planes of (−202), (400), (−603), (310), (−511), (−803) and (020) according to GeP (JCPDS 44–1125). In addition, the XRD peaks at 27.24°, 45.27°, 53.66°, 65.96°, 72.78° and 83.65° can be assigned to the (111), (220), (311), (400), (331) and (422) planes of Ge (JCPDS 04–0545). The Raman scattering spectrum demonstrates the two typical active modes of GeP. The A_g and B_g peaks represent the out-of-plane vibration and in-plane vibration modes, respectively (Fig. 2c) [30]. The vibration peak at 295 cm^{-1} belonging to Ge blue shifts by 5 cm^{-1} compared with the bulk Ge crystal (Fig. S5), indicating the interactions between Ge and GeP as well as the phonon confinement due to the small size of Ge in the Ge/GeP in-plane heterostructure [27]. The chemical composition of the Ge/GeP NSs is determined by XPS which reveals an atomic ratio of Ge to P of about 1.1 (Fig. 2d). Fig. 2e shows the Ge 3*d*

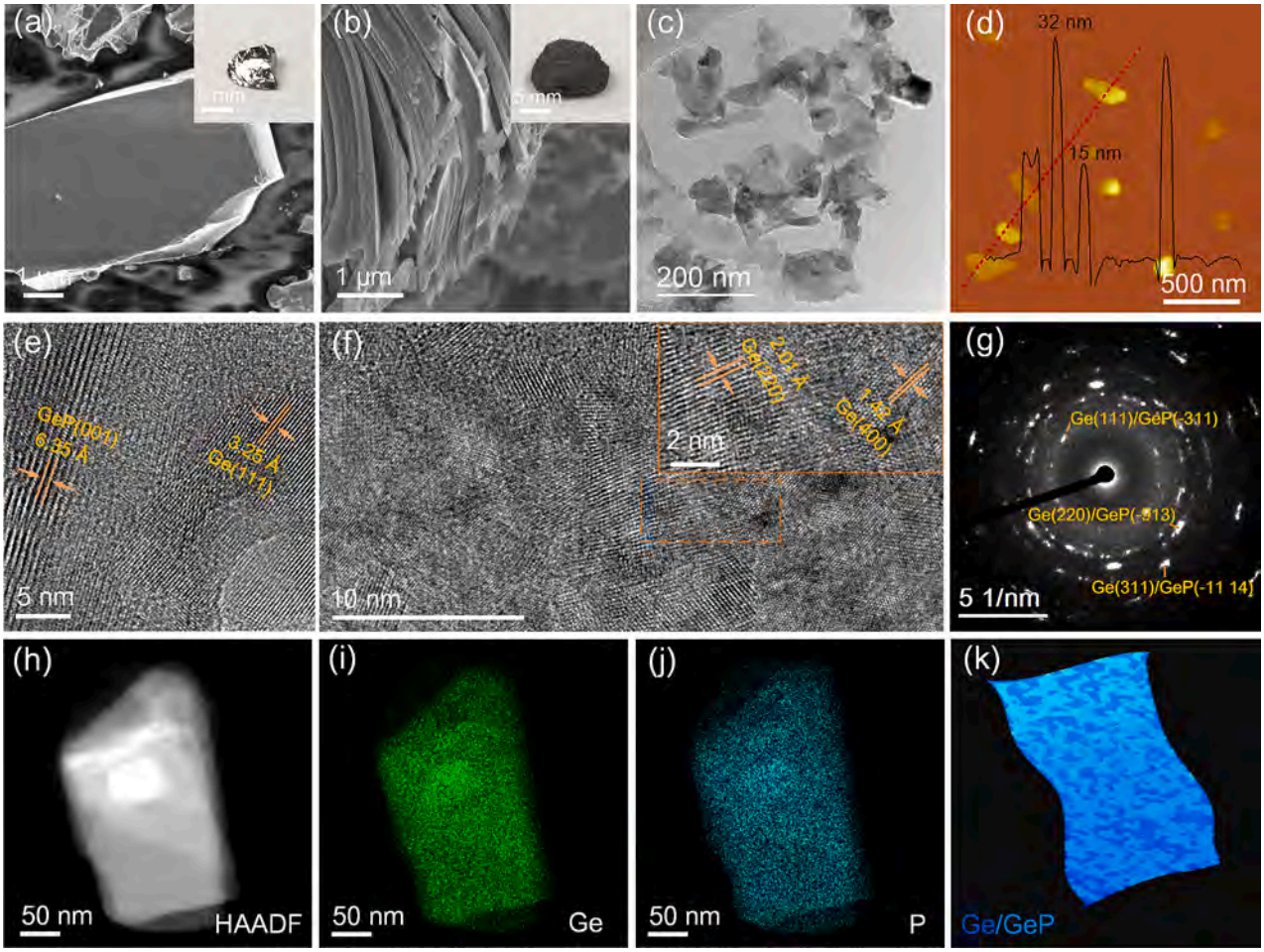

Fig. 1. Characterization of Ge/GeP NSs. (a) SEM image and photograph of Ge crystal. (b) SEM image and photograph of the bulk Ge/GeP crystal. (c) TEM image of the Ge/GeP NSs. (d) AFM image and thickness analysis of the Ge/GeP NSs. (e, f) HR-TEM images and magnified region of the Ge/GeP NS. (g) SAED image. (h-j) HAADF image and elemental maps of one Ge/GeP NS. (k) Schematic diagram of the Ge/GeP in-plane structure.

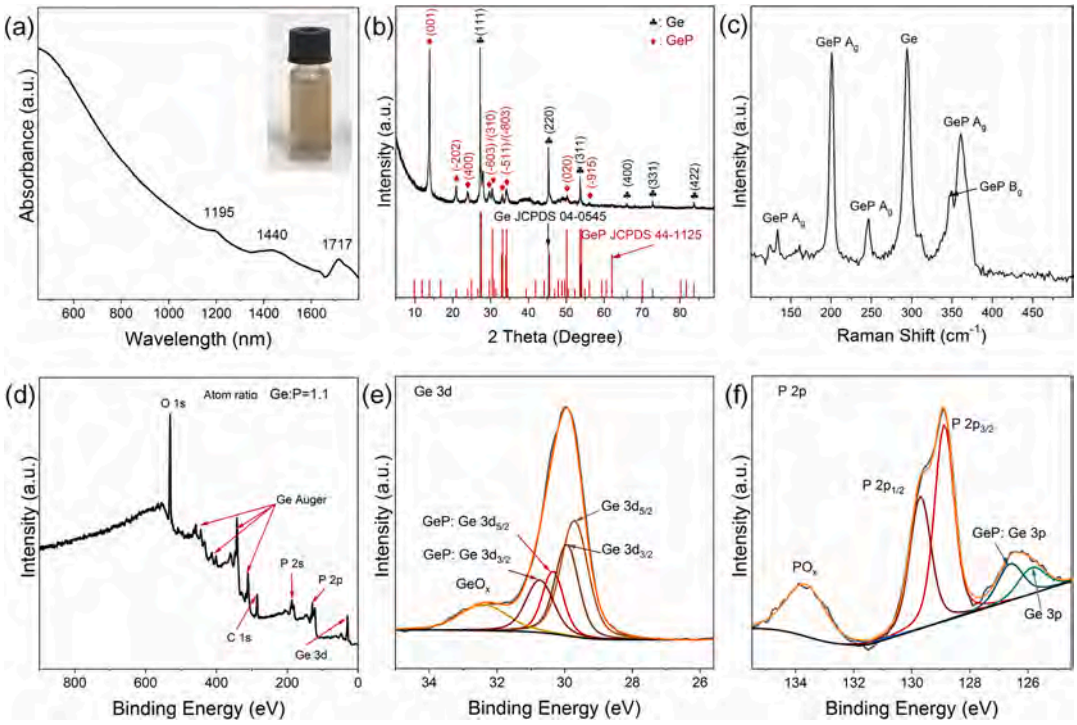

Fig. 2. (a) Solid state diffuse reflectance absorption spectrum and inset photograph of the Ge/GeP NSs in NMP. (b) XRD pattern of the Ge/GeP NSs. (c) Raman scattering spectrum of the Ge/GeP NSs. (d) XPS survey spectrum of Ge/GeP NSs. (e, f) High-resolution XPS spectra of Ge 3*d* and P 2*p*.

spectrum which can be divided to the $3d_{5/2}$ (29.6 eV, 30.3 eV) and $3d_{3/2}$ (30.0 eV, 30.7 eV) doublets of Ge and GeP according to the different valence states of Ge [18,30]. The sub-band at 32.5 eV is probably due to oxidation of Ge during sample preparation and oxidation of P (around 133.7 eV) can be observed from Fig. 2f. The two peaks at 129.0 and 129.7 eV are related to P $2p_{3/2}$ and P $2p_{1/2}$ and the other two peaks at

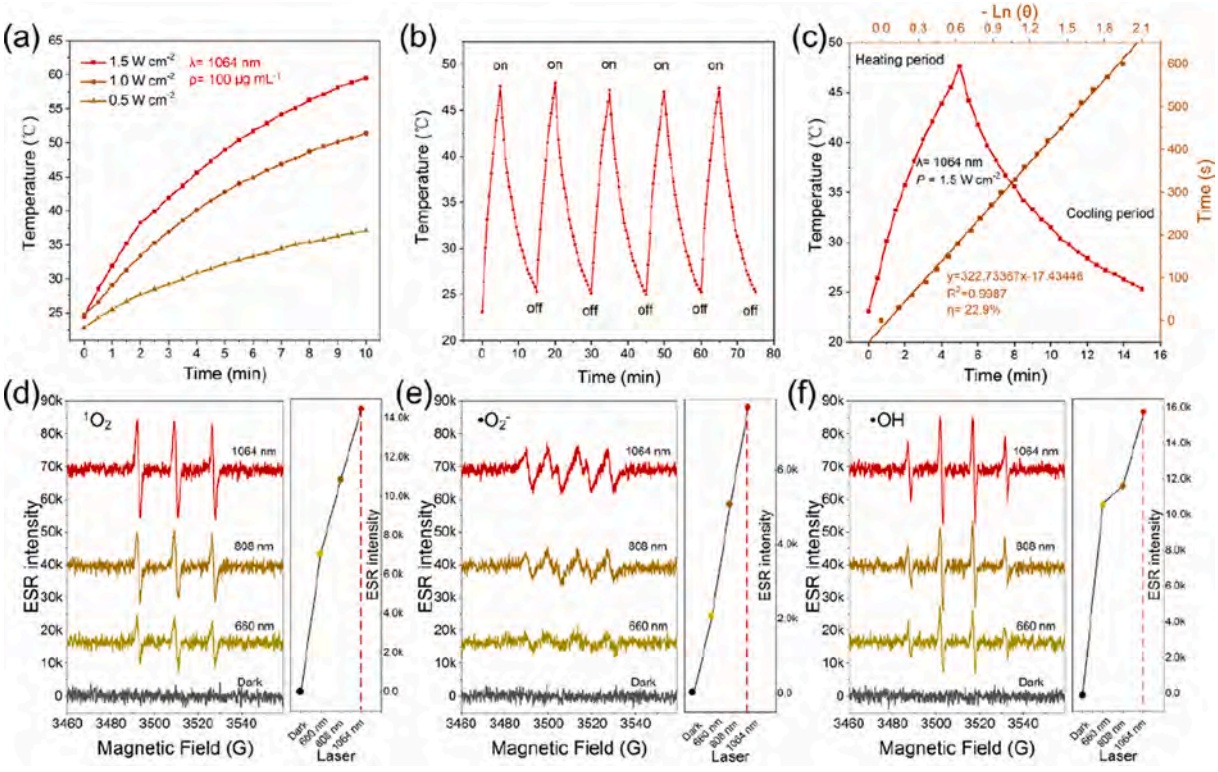

Fig. 3. PTT and PDT characteristics of the Ge/GeP NSs. (a) Photothermal heating curves of the Ge/GeP NSs solution (100 μg mL^{-1}) upon 1,064 nm NIR laser irradiation with power of 0.5, 1.0, and 1.5 W cm^{-2}. (b) Photostability of the Ge/GeP NSs (100 μg mL^{-1}) under 1,064 nm laser irradiation (1.5 W cm^{-2}). (c) Temperature change curve and calculation of the η under 1064 nm laser irradiation. (d-f) $^1O_2$, •O_2^- and •OH generation of Ge/GeP NSs measured by ESR spectra and extracted peak intensity plots under different laser irradiation (Dark, 660, 808 and 1064 nm).

125.8 and 126.5 eV are assigned to Ge 3*p* of Ge and GeP. These results indicate that the compact and high-quality Ge/GeP in-plane heterostructure is fabricated.

3.2. Photothermal and photodynamic effects of Ge/GeP NSs

The NIR optical properties and photothermal properties of the Ge/GeP NSs are investigated. The concentrations of Ge/GeP NSs in the aqueous dispersion are determined by ICP-OES as shown in Fig. S6a. A concentration-dependent absorption intensity and good linearity are observed from the relationship between the normalized absorption intensity at 1,064 nm (A_{1064}/L) and concentration (C) (Fig. S6b). According to Beer-Lambert's Law, the NIR ε of the Ge/GeP NSs at 1,064 nm is 15.66 L/g cm^{-1}, which is much higher than that of other common photothermal agents such as carbon dots modified black phosphorus (4.77 L/g cm^{-1}) [31] and silicon NSs (11.3 L/g cm^{-1}) [32], indicating the Ge/GeP NSs are efficient PTT agents. The photothermal conversion capability of the Ge/GeP NSs in the NIR-II biowindow is studied by monitoring the temperature variations of the dispersions during 1,064 nm laser irradiation. As shown in Fig. S6c and 3a, the temperature of the Ge/GeP NSs dispersions increases quickly depending on the concentration, irradiation time, and power density. For the dispersions with concentrations of 25, 50, and 100 μg mL^{-1}, the temperature reaches 37.3, 42.4 and 51.5 °C within 10 min during irradiation (1.0 W cm^{-2}) but that of deionized water is only 27.7 °C at the same power density (Fig. S6c). The highest temperature of the dispersion (100 μg mL^{-1}) increases by 8.5, 24.7 and 34.8 °C with increasing laser power density (0.5, 1.0 and 1.5 W cm^{-2}), respectively (Fig. 3a). Moreover, neglectable deterioration of the temperature elevation can be observed during five cycles of laser on/off irradiation, suggesting excellent photostability and thermostability (Fig. 3b). These results reveal that the Ge/GeP NSs is a good agent for PTT.

The η of the Ge/GeP NSs at 1,064 nm is calculated to be 22.9% (Fig. 3c) according to previous methods and higher than those of 2D Pd (η = 20% for 1064 nm) [33] and silicon NSs (η = 21.4% for 1064 nm) [32]. The relatively high η of Ge/GeP NSs should be due to the indirect band gap nature and the collision between photoexcited electrons and high-energy phonons during relaxation [24]. The Ge/GeP NSs also show a high ε of 22.54 L/g cm^{-1} and photo-to-heat conversion with η of 29.4% at 808 nm (Fig. S7), which is much higher than that of gold nanorods (η = 21%) [34], bismuthene (η = 19.4%) [35], and traditional grapheme oxide (22%) [36]. Nevertheless, compared to Ge quantum dots (ε = 5.333 L/g cm^{-1}, η = 45.9% for 808 nm) [18] and GeP NSs (ε = 5.83 L/g cm^{-1}, η = 68.6% for 808 nm) [24], the high ε and relatively low η of the Ge/GeP NSs are mismatched, possibly attributable to the special in-plane heterostructure of Ge and GeP components as well as the energy transfer from the Ge/GeP NSs to the surroundings.

Therefore, the photodynamic effects of the Ge/GeP NSs are studied further. ESR was carried out to identify the light triggered ROS species using TEMP as the $^1O_2$ indicator and BMPO as the $\bullet O_2^-$ and •OH indicator [7,37]. As shown in Fig. 3d, the ESR signal from the Ge/GeP NSs during 660 nm laser irradiation shows the 1:1:1 triplet signal characteristic of TEMPO compared to the dark condition, confirming the $^1O_2$ generation (type II PDT) ability under light activation. Enhanced ESR signal intensity is observed with longer NIR wavelength lasers of 808 and 1,064 nm, and the intensity for 1,064 nm is more than twice that for 660 nm, indicating that more $^1O_2$ is generated under 1,064 nm laser irradiation. In addition, BMPO exhibits a sextet signal (Fig. 3e) and a 1:2:2:1 quartet signal (Fig. 3f) under 660 nm laser irradiation, implying that the Ge/GeP NSs can also produce $\bullet O_2^-$ and •OH (type I PDT). Similar to $^1O_2$ generation, upon longer NIR wavelength laser irradiation, larger ESR intensity can be observed for $\bullet O_2^-$ and •OH, suggesting that more $\bullet O_2^-$ and •OH are generated by the Ge/GeP NSs upon 1,064 nm laser irradiation. These results disclose that the Ge/GeP NSs exhibit both type I and type II PDT effects as well as unexpectedly higher ROS generation upon longer NIR wavelength laser irradiation.

According to previous research, Ge is a semiconductor with a work function of 4.8 eV and indirect band gap of ~ 0.67 eV as well as a direct gap of ~ 0.8 eV showing unique optical and electronic properties [38,39]. Owing to the unique electrical structure, Ge nanocrystals have been embedded in many matrices for various applications, for example, carrier extraction, multi-quantum-well active devices, etc [40,41]. GeP is a recently predicted and fabricated indirect semiconductor with great potential in photoelectronic applications [30,42]. First-principle calculation based on the HSE06 functionals reveals that GeP has a tuneable band gap ranging from 0.9 to 2.3 eV (from bulk to single layer) and work function of ~ 4.84 eV for 2D GeP [42,43]. Hence, we suppose the enhanced ROS generation ability observed from the 15–32 nm thick Ge/GeP NSs arises from the heterojunction composed of Ge and GeP with unique optical properties.

To have an in-depth understanding of the charge transfer between Ge and GeP, KPFM was employed to measure the spatial charge distribution in the Ge/GeP in-plane heterostructure. Fig. 4a-c show one representative Ge/GeP sheet with thickness of about 20 nm and the surface potential maps of selected area in darkness and under irradiation. As shown in Fig. 4b, purple and blue colors representing higher and lower potentials can be observed in different regions. The contact potential difference (CPD) between the AFM tip and material area can be written as: CPD $= \varnothing_{tip} - \varnothing_m$, where $\varnothing_{tip}$ and $\varnothing_m$ are the work functions of the tip and test material, respectively. Owing to the work function difference between Ge (4.8 eV) and GeP (4.84 eV), the most purple regions (higher potential) in the KPFM image could be distinguished as Ge and the other blue regions could be GeP (Fig. 4b). Compared to the potential map in darkness, the increase of the blue color regions under irradiation indicates the efficient charge transfer between Ge and GeP (Fig. 4c). Corresponding line-scanning surface potential in Fig. 4d shows that the potential difference between Ge and GeP is about 5 mV in darkness. Upon light irradiation, the surface potential of GeP is further reduced and the potential difference between Ge and GeP enlarges significantly to 16 mV. These results suggest the accumulation of photoexcited electrons on the surface of Ge, which can be attributed to the S-scheme charge-transfer mechanism in the Ge/GeP in-plane heterostructure.

The photocatalytic mechanism for ROS generation is illustrated in Fig. 4e and Fig. S8. Upon light irradiation, electrons are activated in the valence band (VB) of Ge and GeP and then transferred to the conduction band (CB), leaving photogenerated holes in the VB. However, the CB of GeP (-4.4 eV) is close to the chemical potential value of $O_2/\bullet O_2^-$ (-4.454 eV) [37], and so the photoexcited electrons on GeP cannot efficiently react with O_2 to form $\bullet O_2^-$, which is inconsistent with our experimental results. Therefore, the heterojunction of Ge and GeP does not work as a Type-II photocatalyst [44]. Considering that the CB, VB, and Femi level of Ge are all higher than those of GeP and the CB of Ge (-4.13 eV) is higher than the chemical potential of $O_2/\bullet O_2^-$, a more efficient S-scheme heterojunction may be constructed by Ge and GeP due to the special band structure [44,45]. In the S-scheme heterojunction, an internal electric field (IEF) is formed at the interface of the compact Ge and GeP under light irradiation. Driven by the IEF, the photogenerated electrons in the CB of the GeP transfer to the VB of Ge further suppressing the charge-carrier recombination in Ge which is consistent with the KPFM results. Therefore, electrons in the CB of Ge can efficiently react with O_2 to form $\bullet O_2^-$ under light irradiation. The VB of GeP (-5.3 eV) is higher than the chemical potential of $OH^-/\bullet OH$ (-5.9 eV), and holes in the VB of GeP cannot react with OH^- to form •OH. •OH generation can be ascribed to the further evolution of $\bullet O_2^-$ [46]. The $^1O_2$ generation mechanism can be ascribed to absorbed light energy transferred to O_2 and mediated by Ge/GeP NSs, which is similar to that of As NSs and most organic photosensitizers [3,10,47]. It should be noted that enhanced ROS generation under longer wavelength laser irradiation is achieved and this might be due to the synergistic effect of photothermal effect and S-scheme heterojunction. It is known that superior temperature is beneficial to improve the reaction activity in photocatalytic reaction. While extortionate temperature will increase the chance of collision of

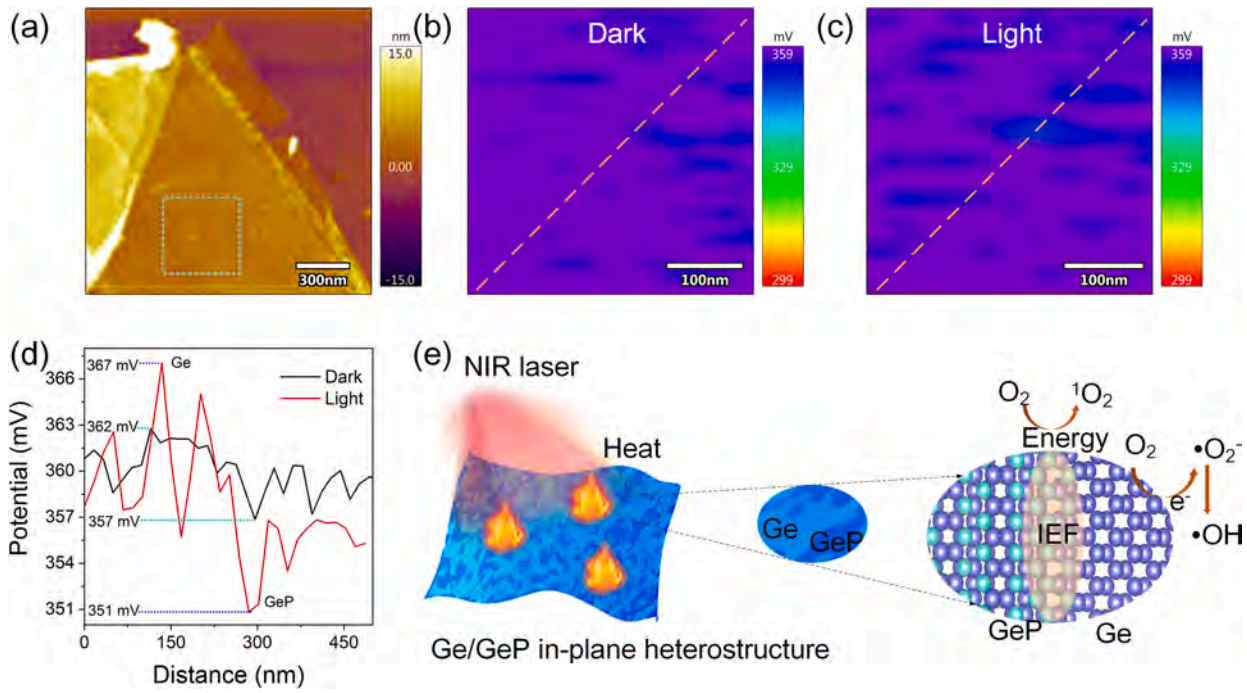

Fig. 4. Charge transport in Ge/GeP in-plane heterostructure. (a) AFM image of one Ge/GeP NS and selected area for KPFM test. (b, c) Corresponding surface potential distribution of selected area in darkness (b) and under light irradiation. (d) The line-scanning surface potential. (e) Schematic introduction for the PTT and PDT activated by NIR laser.

photocarriers in photocatalyst which reduces the photocatalytic activity [48]. To further investigate the ROS generation mechanism, the heating effect of Ge/GeP NSs under different laser irradiation is evaluated. As shown in Fig. S9, the Ge/GeP NSs show a higher heating rate for 660 nm than 808 and 1,064 nm, indicating a contrary tendency compared with the ROS generation tendency under laser irradiation. Under longer wavelength laser irradiation, the η reduces while the ROS generation is greatly enhanced (Fig. 3d-f), suggesting that the recombination of photogenerated carriers under longer wavelength laser irradiation is weakened and there is a balance between the local temperature and the photocatalytic activity on the surface of Ge/GeP NSs. Compared to the photothermal and photodynamic effects of Ge/GeP NSs under 808 nm, the Ge/GeP NSs under 1064 nm retain 77.9% of η and achieve enhanced ROS generation of 133% for $^1O_2$, 151% for $\bullet O_2^-$ and 135% for •OH, respectively. Moreover, 1064 nm laser endows higher permissible exposure and greater penetration depth [2–5]. Thus, the Ge/GeP NS with acceptable η and outstanding ROS generation ability is a promising PTA candidate under 1064 nm.

3.3. Degradability and biocompatibility of the Ge/GeP NSs

The degradation behavior of the Ge/GeP NSs is inferred from the absorption spectra (Fig. S10a). As the Ge/GeP NSs are stored in water, the absorption intensity decreases gradually from 0 to 27 days, indicating possible degradation. TEM is used to confirm the degradability and as shown in Fig. S10b-d, the Ge/GeP NSs become more transparent after 3 days and the characteristic 2D planar structure of the original nanosheets is broken into small pieces after 9 days. Therefore, the natural degradation of Ge-based NSs in the aqueous solution is corroborated. The dispersity of the Ge/GeP NSs in different media is investigated. As shown in Fig. S11, the Ge/GeP NSs exhibit great dispersity in water, DMEM/10% FBS, serum-free RPMI1640, and RPMI1640/10% FBS even after 24 h. Although the Ge/GeP NSs in the PBS and DMEM precipitate after 24 h, those in PBS and DMEM display no obvious agglomeration in 1 h and only slight aggregation after 4 h. These results show the Ge/GeP NSs have the desirable dispersity and stability in physiological solutions.

Efficient cellular uptake and good biocompatibility are vital to biomedical applications. Therefore, the cell uptake behavior is examined by cultivating HeLa and MCF-7 cells with the Ge/GeP NSs for 4 h at 37 °C. As shown in Fig. S12a-f, compared to the groups without Ge/GeP NSs, those with Ge/GeP NSs show a significant amount of trapped particles which enter the cells mainly by endocytosis. Owing to the strong Raman sensitivity of Ge/GeP NSs, these particles can be easily distinguished by Raman scattering. The potential cytotoxicity of the Ge/GeP NSs towards normal and tumor cells is then investigated by flow cytometry (Fig. S12g). After incubation with the Ge/GeP NSs for 24 h with a pre-designed concentration of 100 μg mL^{-1}, the cell viabilities of Hela, MCF-7 and QSG-7701 cells are 86.7%, 93.0% and 87.5%, respectively, indicating no significant cytotoxicity compared to the controls without Ge/GeP NSs.

3.4. Synergistic phototherapeutic effects of Ge/GeP NSs in vitro and in vivo

Considering the superior optical properties and excellent ROS generation ability of Ge/GeP NSs, the effects of *in vitro* PDT is evaluated. Intracellular ROS generation is measured with DCFH-DA as the fluorescent probe [7]. As shown in Fig. 5a, there is negligible green fluorescence from all the control groups including the control group (untreated cells), only laser irradiated group and only Ge/GeP NSs treated group for both HeLa and MCF-7 cells. After incubation with Ge/GeP NSs and 1,064 nm laser irradiation at 1.0 W cm^{-2} for 1, 3 and 5 min, gradually increased green fluorescence is observed indicative of efficient ROS generation.

To further demonstrate the synergistic phototherapeutic effects of PTT and PDT *in vitro*, calcein AM and PI co-staining analysis is conducted. In the absence of laser irradiation and Ge/GeP NSs, all the cells exhibit green fluorescence, indicating that the Ge/GeP NSs have negligible toxicity (Fig. 5b) in agreement with Fig. S12g. In contrast, strong concentration-dependent red fluorescence can be observed and almost all the Hela or MCF-7 cells are killed after 1,064 nm laser irradiation for

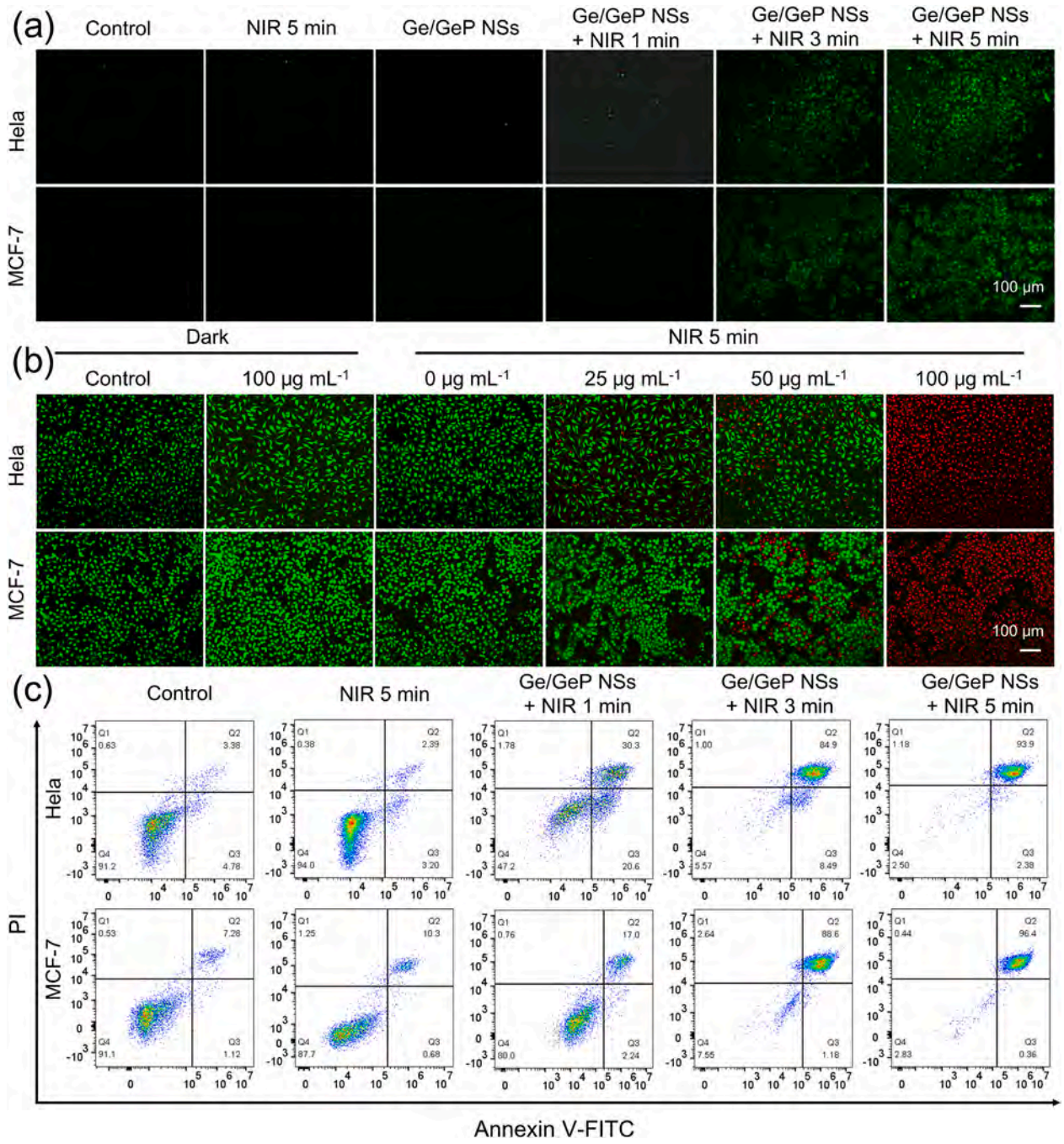

Fig. 5. Cell experiments *in vitro*. (a) Intracellular ROS detection using DCFH-DA as the probe. (b) Fluorescence images of the Ge/GeP NSs treated Hela and MCF-7 cells after 1,064 nm laser irradiation with the cells co-stained with calcein AM (green, live cells) and PI (red, dead cells). (c) Cell apoptosis monitored by flow cytometry.

5 min at the concentration of 100 μg mL^{-1} of the Ge/GeP NSs for a power density of 1.0 W cm^{-2}. The optimal parameters of effective phototherapy *in vitro* are investigated. Laser ablation of cancer cells is carried out at different time (1, 3, 5 min) and power densities (0.5, 1.0, 1.5 W cm^{-2}). As shown in Fig. S13, efficient cancer cell killing is achieved by 1,064 nm laser irradiation for 3 min at a power density of 1.0 W cm^{-2}, further confirming the strong phototoxicity of Ge/GeP NSs towards cancer cells. Flow cytometric analysis is performed to investigate the cell apoptosis and necrosis mechanisms (Fig. 5c). 94.0% of Hela cell and 87.7% of MCF-7 cell viabilities are observed from the NIR treated group. However, the early apoptosis rate of the Hela cells reaches 20.6% and the late apoptosis rate is 30.3% after 1,064 nm laser irradiation of the Ge/GeP NSs treated group for 1 min. As the irradiation time is extended to 3 min, the late apoptosis rate increases remarkably to 84.9% which is close to saturation. When the irradiation time is further extended to 5 min, the late apoptosis rate increases slowly and this tendency can be observed from the phototherapy experiment of MCF-7 cells *in vitro*. Therefore, cell death caused by phototherapy with Ge/GeP NSs is mainly achieved by cell apoptosis. These results indicate that the Ge/GeP NSs possess highly efficient PTT and type I, type II PDT synergistic therapeutic effects boasting superiority in single NIR-II laser activation, less irradiation time, and lower laser power compared to other strategies summarized in Table S1.

Encouraged by the excellent *in vitro* PTT/PDT synergistic anticancer effects, the *in vivo* PTT/PDT synergistic therapeutic ability of the Ge/GeP NSs is assessed using the animal model of MCF-7-tumor-bearing BALB/c

nude mice. Four randomly divided groups including the control group (PBS), Ge/GeP NSs-treated group, NIR-treated group (PBS + NIR) and Ge/GeP NSs + NIR-treated group are formed and different treatments are carried out when the size of the tumors reaches 250 mm^3. After intratumor administration, the mice are anesthetized and exposed to the 1,064 nm NIR laser at a power density of 1.0 W cm^{-2}. The thermal data are recorded by an infrared thermal camera (Fig. 6a, b). The temperature at the tumor site increases rapidly to ~ 60 °C within 4 min for the Ge/GeP NSs + NIR-treated group. In comparison, the tumor temperature of the NIR-treated group only increases by about 10 °C within 4 min. The results suggest the remarkable photothermal effects of Ge/GeP NSs *in vivo* verifying that the Ge/GeP NSs are excellent for type I, type II PDT synergistic anticancer treatment.

After the different treatments, the tumor growth is monitored to further confirm the therapeutic efficiency. No abnormal weight loss is observed from all mice during the treatment period (Fig. 6c) indicating high biocompatibility and negligible side effects. As shown in Fig. 6d-f, at 14 days after treatment, mitigated tumor growth is observed from the Ge/GeP NSs + NIR group. In contrast, significant tumor growth is observed from other three mice groups, demonstrating that only NIR laser or Ge/GeP NSs treatment cannot suppress tumor growth. The Ge/GeP NSs show the PTT and type I, type II PDT synergetic antitumor effect. The *in vivo* anticancer mechanism is examined by H&E staining, TUNEL staining, and Ki-67 immunohistochemistry staining, respectively (Fig. 6g). H&E staining shows severe necrosis in the Ge/GeP NSs + NIR group and almost no TUNEL-positive cells (red) are observed in the control group, Ge/GeP NSs-treated group and NIR-treated group. In contrast, significant colocalization of the nuclei (DAPI staining, blue) and TUNEL-positive apoptotic cells (red) are observed from the Ge/GeP NSs + NIR group, suggesting that Ge/GeP NSs-mediated type I and type II PDT can activate apoptosis to induce intratumoral cell death. Moreover, positive Ki-67 staining exhibits strong suppression effects on cell roliferation and more severe apoptotic levels in the Ge/GeP NSs + NIR group compared to the other groups. To further evaluate the *in vivo* toxicity of Ge/GeP NSs with 1,064 nm laser phototherapy, the mice with different treatments are sacrificed on the 14th day post-injection. The

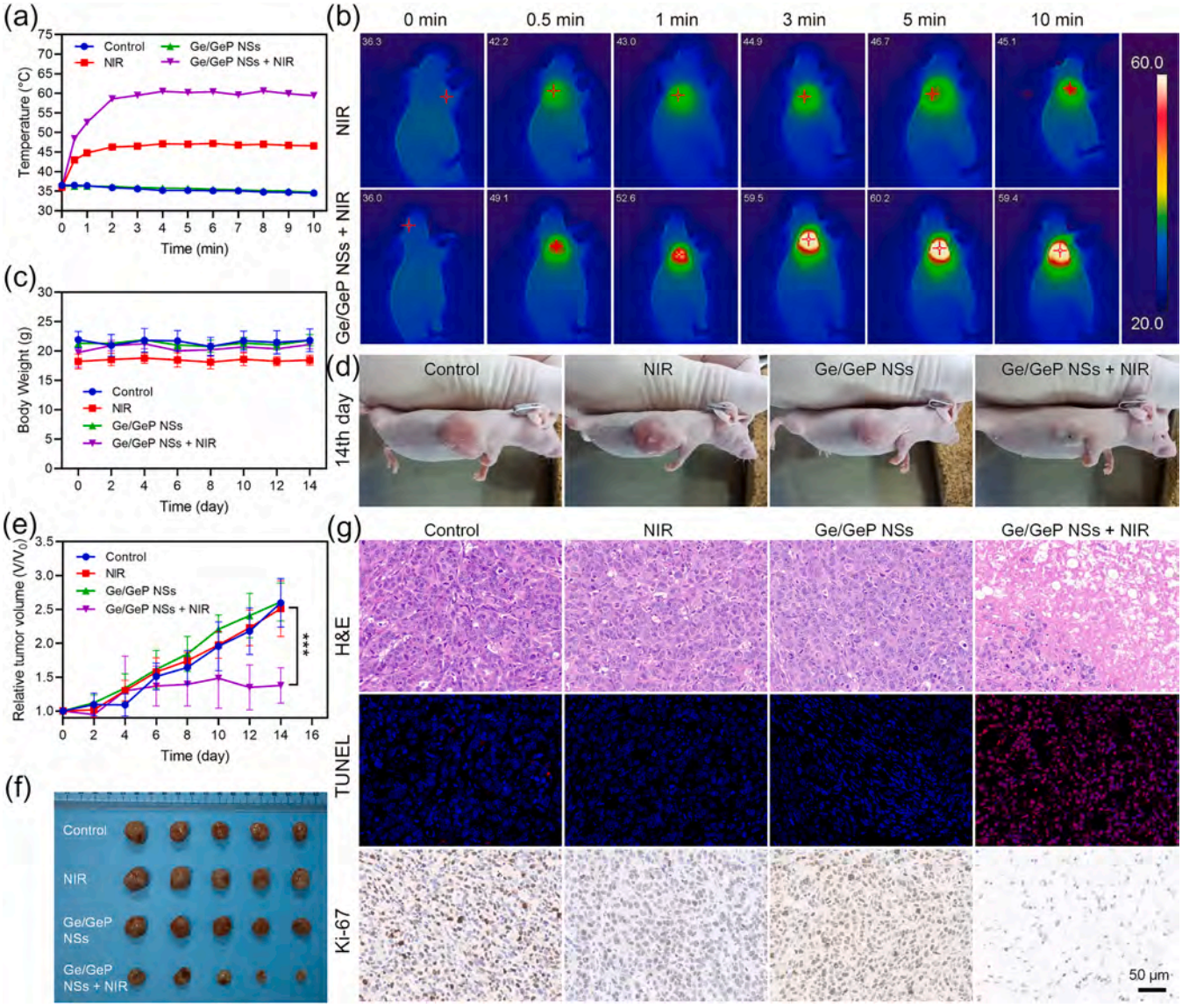

Fig. 6. Synergistic anticancer experiments *in vivo*. (a) Temperature variations at the tumor sites in the MCF-7-tumor-bearing mice of different groups (Control, NIR, Ge/GeP NSs, and Ge/GeP NSs + NIR) during NIR laser (1064 nm, 1.0 W cm^{-2}) irradiation. (b) IR thermal images acquired at different time intervals. (c) Time-dependent body weights of the mice after different treatments (n = 5). (d) Photographs of the MCF-7-tumor-bearing mice and tumor regions of different groups after 14 days. (e) Time-dependent tumor growth curves (n = 5, mean ± SD) after the different treatments. Statistical P-values: $^*P < 0.05$, $^{**}P < 0.01$, $^{***}P < 0.001$. (f) Photographs of the tumors extracted from the mice in different groups after 14 days. (g) H&E, TUNEL, and Antigen Ki-67 analysis of the tumor slices.

main organs (heart, liver, spleen, lung, and kidney) are collected and stained with H&E for histological examination (Fig. S14), while blood is collected for the hematological and blood biochemical analysis (Fig. S15). According to H&E staining, no noticeable histological abnormality is observed from the normal tissues, indicating that the Ge/GeP NSs and laser have negligible toxicity or side effects on the healthy tissues (Fig. S14). Moreover, the standard blood biochemical indexes of aspartate transaminase (AST), total protein (TP), globulin (GLB), total bilirubin (TBIL), blood urea nitrogen (BUN), creatinine (CREA), and albumin (ALB) in the Ge/GeP NSs-treated group, NIR-treated group or Ge/GeP NSs + NIR-treated group show no abnormity in comparison to the control group and the changes are of no statistical significance (Fig. S15). In particular, AST and CREA are related functional indexes for the kidney and liver and the levels indicate that the Ge/GeP NSs induce no significant renal and hepatic toxicity thus having negligible toxicity in the biological system. These results demonstrate that the Ge/GeP NSs are efficient PTT and type I, type II PDT synergetic antitumor PTAs with excellent biocompatibility.

4. Conclusions

Inspired by the previously reported bifunctional PTAs [2–13], in this work, a 2D sheet-like and compact S-scheme Ge/GeP in-plane heterostructure is designed for cancer therapy. The 2D sheet-like Ge/GeP NSs with a thickness of 15 to 32 nm and lateral size of 153 ± 39 nm are synthesized by a top-down approach involving grinding and sonication using the bulk materials produced by the CVT method. During the CVT process, none-layered Ge is transformed to layered Ge/GeP structure and thus the Ge/GeP NSs can be easily exfoliated. The polycrystalline surface nature as well as in-plane heterostructure of Ge/GeP NS is confirmed. The Ge/GeP NSs have a large ε of 15.66 L/g cm^{-1} at 1,064 nm and high η of 22.9% upon 1,064 nm laser irradiation [31–33]. Moreover, both type I and type II PDT are activated from the Ge/GeP NSs with a single laser and enhanced ROS generation is observed during longer NIR wavelength laser irradiation, which has not been reported on Ge-based materials [18,20,24,43]. The ESR intensity of $^1O_2$ and $\bullet O_2^-$ under 1,064 nm laser irradiation is more than double that under 660 nm laser irradiation and this might be due to the synergistic effect of photothermal effect and S-scheme heterojunction [48].The S-scheme charge transfer mechanism between Ge and GeP is investigated by photo-irradiated KPFM and ESR analysis. The formation of such S-scheme Ge/GeP heterostructure endows the Ge/GeP NS-based PTA with boosted charge separation on the surface. In addition, the Ge/GeP NSs have the desirable dispersity and stability in physiological solutions as well as degradability. As a result, the Ge/GeP NSs show outstanding synergistic therapeutic effects of PTT/PDT both *in vitro* and *in vivo* in the NIR-II biowindow besides excellent biocompatibility. This nanoplatform has large clinical potential and the results provide insights into the design of efficient PTAs with high η and surface activity.

CRediT authorship contribution statement

Xianwei Mo: Investigation, Methodology, Writing – original draft. **Hao Huang:** Conceptualization, Supervision, Writing – original draft, Writing – review & editing, Funding acquisition. **Caixia Sun:** Investigation. **Zhenyu Zhang:** Methodology. **Jiahong Wang:** Formal analysis, Funding acquisition, Writing – original draft. **Shengyong Geng:** Formal analysis, Writing – original draft. **Paul K. Chu:** Writing – review & editing, Funding acquisition. **Xue-Feng Yu:** Writing – review & editing, Funding acquisition. **Wenxin Liu:** Conceptualization, Writing – review & editing, Supervision, Project administration, Funding acquisition.

Declaration of Competing Interest

The authors declare that they have no known competing financial interests or personal relationships that could have appeared to influence the work reported in this paper.

Data availability

Data will be made available on request.

Acknowledgements

This work was supported by the General Program of Natural Science Foundation of Guangdong Province (2020A1515010639, W.L.; 2022A1515011959, H.H.), Science and technology special competitive allocation project of Zhanjiang City (2021A05147, W.L.; 2021A05130 X.M.), Ph.D Start-up Program of Central People's Hospital of Zhanjiang (2020A07, W.L.), Young Elite Scientist Sponsorship Program by CAST (No. YESS20210226, J.W.), Youth Innovation Promotion Association Chinese Academy of Sciences (2020354, J.W.), City University of Hong Kong Donation Research Grant (DON-RMG 9229021, P.C.), City University of Hong Kong Donation Grant (9220061, P.C.), Hong Kong PDFS-RGC Postdoctoral Fellowship Scheme (PDFS2122-1S08 and CityU 9061014, P.C.), and Hong Kong HMRF (Health and Medical Research Fund) (2120972 and CityU 9211320, P.C.). All the animal experiments were conducted in accordance with the guidelines from and approved by Wuhan Servicebio Technology Co., Ltd., China and the ethical approval protocol number was Servicebio Animal Welfare No. 2022011.

Appendix A. Supplementary material

Supplementary data to this article can be found online at https://doi.org/10.1016/j.jcis.2023.08.137.

References

[1] Z. Xie, T. Fan, J. An, W. Choi, Y. Duo, Y. Ge, B. Zhang, G. Nie, N. Xie, T. Zheng, Y. Chen, H. Zhang, J.S. Kim, Emerging combination strategies with phototherapy in cancer nanomedicine, Chem. Soc. Rev. 49 (22) (2020) 8065–8087.
[2] C. Xu, K. Pu, Second near-infrared photothermal materials for combinational nanotheranostics, Chem. Soc. Rev. 50 (2) (2021) 1111–1137.
[3] K. Wen, H. Tan, Q. Peng, H. Chen, H. Ma, L. Wang, A. Peng, Q. Shi, X. Cai, H. Huang, Achieving efficient NIR-II type-I photosensitizers for photodynamic/photothermal therapy upon regulating chalcogen elements, Adv. Mater. 34 (7) (2022) 2108146.
[4] S. Wang, H. Chen, J. Liu, C. Chen, B. Liu, NIR-II light activated photosensitizer with aggregation-induced emission for precise and efficient two-photon photodynamic cancer cell ablation, Adv. Funct. Mater. 30 (30) (2020) 2002546.
[5] D. An, J. Fu, B. Zhang, N. Xie, G. Nie, H. Ågren, M. Qiu, H. Zhang, NIR-II responsive inorganic 2D nanomaterials for cancer photothermal therapy: recent advances and future challenges, Adv. Funct. Mater. 31 (32) (2021) 2101625.
[6] S. Liu, X. Pan, H. Liu, Two-dimensional nanomaterials for photothermal therapy, Angew. Chem. Int. Ed. 59 (15) (2020) 5890–5900.
[7] L. Feng, C. Li, L. Liu, Z. Wang, Z. Chen, J. Yu, W. Ji, G. Jiang, P. Zhang, J. Wang, B. Z. Tang, Acceptor planarization and donor rotation: A facile strategy for realizing synergistic cancer phototherapy via type I PDT and PTT, ACS Nano 16 (3) (2022) 4162–4174.
[8] M. Li, J. Xia, R. Tian, J. Wang, J. Fan, J. Du, S. Long, X. Song, J.W. Foley, X. Peng, Near-infrared light-initiated molecular superoxide radical generator: rejuvenating photodynamic therapy against hypoxic tumors, J. Am. Chem. Soc. 140 (44) (2018) 14851–14859.
[9] J. An, S. Tang, G. Hong, W. Chen, M. Chen, J. Song, Z. Li, X. Peng, F. Song, W.-H. Zheng, An unexpected strategy to alleviate hypoxia limitation of photodynamic therapy by biotinylation of photosensitizers, Nat. Commun. 13 (1) (2022) 2225.
[10] T. Luo, K. Ni, A. Culbert, G. Lan, Z. Li, X. Jiang, M. Kaufmann, W. Lin, Nanoscale metal–organic frameworks stabilize bacteriochlorins for type I and type II photodynamic therapy, J. Am. Chem. Soc. 142 (16) (2020) 7334–7339.
[11] Y. Zhang, Y. Cheng, F. Yang, Z. Yuan, W. Wei, H. Lu, H. Dong, X. Zhang, Near-infrared triggered Ti_3C_2/g-C_3N_4 heterostructure for mitochondria-targeting multimode photodynamic therapy combined photothermal therapy, Nano Today 34 (2020), 100919.
[12] W. Sun, H. Yu, D. Wang, Y. Li, B. Tian, S. Zhu, P.-Y. Wang, S. Xie, R. Wang, MnO_2 nanoflowers as a multifunctional nano-platform for enhanced photothermal/photodynamic therapy and MR imaging, Biomater. Sci-UK 9 (10) (2021) 3662–3674.
[13] Y. Wang, J. Zhao, Z. Chen, F. Zhang, Q. Wang, W. Guo, K. Wang, H. Lin, F. Qu, Construct of $MoSe_2$/Bi_2Se_3 nanoheterostructure: Multimodal CT/PT imaging-guided PTT/PDT/chemotherapy for cancer treating, Biomaterials 217 (2019), 119282.

[14] W. Zhang, J.-B. You, J. Liu, X. Xiong, Z. Li, C.E. Png, L. Wu, C.-W. Qiu, Z.-K. Zhou, Steering room-temperature plexcitonic strong coupling: A diexcitonic perspective, Nano Lett. 21 (2021) 8979–8986.
[15] X. Cai, Y. Luo, B. Liu, H.M. Cheng, Preparation of 2D material dispersions and their applications, Chem. Soc. Rev. 47 (16) (2018) 6224–6266.
[16] Z. Sun, H. Xie, S. Tang, X.F. Yu, Z. Guo, J. Shao, H. Zhang, H. Huang, H. Wang, P. K. Chu, Ultrasmall black phosphorus quantum dots: Synthesis and use as photothermal agents, Angew. Chem. Int. Ed. Engl. 54 (39) (2015) 11526–11530.
[17] Z. Xie, Y. Duo, T. Fan, Y. Zhu, S. Feng, C. Li, H. Guo, Y. Ge, S. Ahmed, W. Huang, H. Liu, L. Qi, R. Guo, D. Li, P.N. Prasad, H. Zhang, Light-induced tumor theranostics based on chemical-exfoliated borophene, Light-Sci. Appl. 11 (1) (2022) 324.
[18] J. Ouyang, C. Feng, X. Ji, L. Li, H.K. Gutti, N.Y. Kim, D. Artzi, A. Xie, N. Kong, Y.-N. Liu, G.J. Tearney, X. Sui, W. Tao, O.C. Farokhzad, 2D monoelemental germanene quantum dots: Synthesis as robust photothermal agents for photonic cancer nanomedicine, Angew. Chem. Int. Ed. 58 (38) (2019) 13405–13410.
[19] W. Chen, J. Ouyang, H. Liu, M. Chen, K. Zeng, J. Sheng, Z. Liu, Y. Han, L. Wang, J. Li, L. Deng, Y.N. Liu, S. Guo, Black phosphorus nanosheet-based drug delivery system for synergistic photodynamic/photothermal/chemotherapy of cancer, Adv. Mater. 29 (5) (2017) 1603864.
[20] C. Feng, J. Ouyang, Z. Tang, N. Kong, Y. Liu, L. Fu, X. Ji, T. Xie, O.C. Farokhzad, W. Tao, Germanene-based theranostic materials for surgical adjuvant treatment: inhibiting tumor recurrence and wound infection, Matter 3 (1) (2020) 127–144.
[21] X. Li, Y. Liu, F. Fu, M. Cheng, Y. Liu, L. Yu, W. Wang, Y. Wan, Z. Yuan, Single NIR laser-activated multifunctional nanoparticles for cascaded photothermal and oxygen-independent photodynamic therapy, Nano-Micro Lett. 11 (1) (2019) 68.
[22] Q. Wu, G. Chen, K. Gong, J. Wang, X. Ge, X. Liu, S. Guo, F. Wang, MnO_2-laden black phosphorus for MRI-guided synergistic PDT, PTT, and chemotherapy, Matter 1 (2) (2019) 496–512.
[23] Q. Zhan, X. Shi, B. Jiang, Y. Zheng, L. Zhou, P. Cao, S. Wei, Two-dimensional polydopamine fabrication by a mild oxidation-based exfoliation route and its application for cancer treatment, Adv. Mater. Inter. 9 (20) (2022) 2200440.
[24] X. Ren, W. Liu, H. Zhou, J. Wei, C. Mu, Y. Wan, X. Yang, A. Nie, Z. Liu, X. Yang, Z. Luo, Biodegradable 2D GeP nanosheets with high photothermal conversion efficiency for multimodal cancer theranostics, Chem. Eng. J. 431 (2022), 134176.
[25] D. Wang, F. Luo, M. Lu, X. Xie, L. Huang, W. Huang, Chemical vapor transport reactions for synthesizing layered materials and their 2D counterparts, Small 15 (40) (2019) 1804404.
[26] P. Zhang, X.F. Lu, D. Luan, X.W. Lou, Fabrication of heterostructured Fe_2TiO_5-TiO_2 nanocages with enhanced photoelectrochemical performance for solar energy conversion, Angew. Chem. Int. Ed. 59 (21) (2020) 8128–8132.
[27] J.R. Heath, J.J. Shiang, A.P. Alivisatos, Germanium quantum dots: Optical properties and synthesis, J. Chem. Phys. 101 (2) (1994) 1607–1615.
[28] C. Bostedt, T. van Buuren, T.M. Willey, N. Franco, L.J. Terminello, C. Heske, T. Möller, Strong quantum-confinement effects in the conduction band of germanium nanocrystals, Appl. Phys. Lett. 84 (20) (2004) 4056–4058.
[29] I. Millo, D. Balberg, T.K. Azulay, A.K. Purkait, E. Swarnakar, J.G.C. Rivard, Veinot, Direct evaluation of the quantum confinement effect in single isolated Ge nanocrystals, J. Phys. Chem. Lett. 6 (17) (2015) 3396–3402.
[30] T. Yu, H. Nie, S. Wang, B. Zhang, S. Zhao, Z. Wang, J. Qiao, B. Han, J. He, X. Tao, Two-dimensional GeP-based broad-band optical switches and photodetectors, Adv. Opt. Mater. 8 (2) (2020) 1901490.
[31] B. Geng, W. Shen, P. Li, F. Fang, H. Qin, X.K. Li, D. Pan, L. Shen, Carbon dot-passivated black phosphorus nanosheet hybrids for synergistic cancer therapy in the NIR-II Window, ACS Appl. Mater. Inter. 11 (48) (2019) 44949–44960.
[32] Z. Cheng, H. Cui, Q. Xiao, H. Huang, Y. Kang, Q. Liu, J. Wang, P.K. Chu, From octahedron crystals to 2D silicon nanosheets: Facet-selective cleavage and biophotonic applications, Small 16 (45) (2020) 2003594.
[33] L. Zhang, S. Li, X. Chen, T. Wang, L. Li, Z. Su, C. Wang, Tailored surfaces on 2D material: UFO-like cyclodextrin-Pd nanosheet/metal organic framework janus nanoparticles for synergistic cancer therapy, Adv. Funct. Mater. 28 (51) (2018) 1803815.
[34] C.M. Hessel, V.P. Pattani, M. Rasch, M.G. Panthani, B. Koo, J.W. Tunnell, B. A. Korgel, Copper selenide nanocrystals for photothermal therapy, Nano Lett. 11 (6) (2011) 2560–2566.
[35] Y. Wang, W. Feng, M. Chang, J. Yang, Y. Guo, L. Ding, L. Yu, H. Huang, Y. Chen, J. Shi, Engineering 2D multifunctional ultrathin bismuthene for multiple photonic nanomedicine, Adv. Funct. Mater. 31 (6) (2021) 2005093.
[36] C.-W. Lo, D. Zhu, H. Jiang, An infrared-light responsive graphene-oxide incorporated poly(N-isopropylacrylamide) hydrogel nanocomposite, Soft Matter 7 (12) (2011) 5604–5609.
[37] M. Qiu, D. Wang, H. Huang, T. Yin, W. Bao, B. Zhang, Z. Xie, N. Xie, Z. Wu, C. Ge, Q. Wang, M. Gu, H.L. Kutscher, L. Liu, S. Bao, P.N. Prasad, H. Zhang, A regioselectively oxidized 2D Bi/BiO_x lateral nano-heterostructure for hypoxic photodynamic therapy, Adv. Mater. 33 (49) (2021) 2102562.
[38] G.W. Gobeli, F.G. Allen, Photoelectric properties of cleaved GaAs, GaSb, InAs, and InSb surfaces; Comparison with Si and Ge, Phys. Rev. 137 (1A) (1965). A245-A254.
[39] H. Garcia, K.N. Avanaki, Direct and indirect two-photon absorption in Ge within the effective mass approximation, Appl. Phys. Lett. 100 (13) (2012), 131105.
[40] T. Tayagaki, N. Usami, W. Pan, Y. Hoshi, K. Ooi, Y. Kanemitsu, Enhanced carrier extraction from Ge quantum dots in Si solar cells under strong photoexcitation, Appl. Phys. Lett. 101 (13) (2012), 133905.
[41] P. Chaisakul, D. Marris-Morini, J. Frigerio, D. Chrastina, M.-S. Rouifed, S. Cecchi, P. Crozat, G. Isella, L. Vivien, Integrated germanium optical interconnects on silicon substrates, Nat. Photonics 8 (6) (2014) 482–488.
[42] H. Zeng, R.-S. Chen, G. Yao, Tunable electronic properties and potential applications of 2D GeP/graphene van der Waals heterostructure, Adv. Electron. Mater. 6 (3) (2020) 1901024.
[43] D. Kim, K. Park, F. Shojaei, T.T. Debela, I.S. Kwon, I.H. Kwak, J. Seo, J.P. Ahn, J. Park, H.S. Kang, Thickness-dependent bandgap and electrical properties of GeP nanosheets, J. Mater. Chem. A 7 (27) (2019) 16526–16532.
[44] Q. Xu, L. Zhang, B. Cheng, J. Fan, J. Yu, S-scheme heterojunction photocatalyst, Chem 6 (7) (2020) 1543–1559.
[45] L. Wang, C. Bie, J. Yu, Challenges of Z-scheme photocatalytic mechanisms, Trends in Chemistry 4 (11) (2022) 973–983.
[46] H. Kisch, Semiconductor photocatalysis-mechanistic and synthetic aspects, Angew. Chem. Int. Ed. 52 (3) (2013) 812–847.
[47] N. Kong, H. Zhang, C. Feng, C. Liu, Y. Xiao, X. Zhang, L. Mei, J.S. Kim, W. Tao, X. Ji, Arsenene-mediated multiple independently targeted reactive oxygen species burst for cancer therapy, Nat. Commun. 12 (1) (2021) 4777.
[48] M. Li, J. Sun, G. Chen, S. Wang, S. Yao, Inducing photocarrier separation via 3D porous faveolate cross-linked carbon to enhance photothermal/pyroelectric property, Adv. Powder Mater. 1 (2022), 100032.

Synthesis of Germanium/Germanium Phosphide in-Plane Heterostructure with Efficient Photothermal and Enhanced Photodynamic Effects in the Second Near-Infrared Biowindow

*Xianwei Mo [a], Hao Huang [b *], Caixia Sun [b, d], Zhenyu Zhang [b], Jiahong Wang [b, c], Shengyong Geng [b], Paul K. Chu [e], Xue-Feng Yu [b, c], and Wenxin Liu [a *]*

[a] *Zhanjiang Institute of Clinical Medicine, Zhanjiang Central Hospital, Guangdong Medical University, Zhanjiang, 524045, China*

[b] *Shenzhen Key Laboratory of Micro/Nano Biosensing, Shenzhen Institute of Advanced Technology, Chinese Academy of Sciences, Shenzhen, 518055, China*

[c] *Hubei Three Gorges Laboratory, Yichang, Hubei, 443007, China*

[d] *The First Clinical Medical School, Guangdong Medical University, Zhanjiang, 524023, China*

[e] *Department of Physics, Department of Materials Science and Engineering, and Department of Biomedical Engineering, City University of Hong Kong, Tat Chee Avenue, Kowloon, Hong Kong, China*

***Corresponding authors.**

E-mail: wenxin_liu@gdmu.edu.cn (W. Liu); hao.huang@siat.ac.cn (H. Huang)

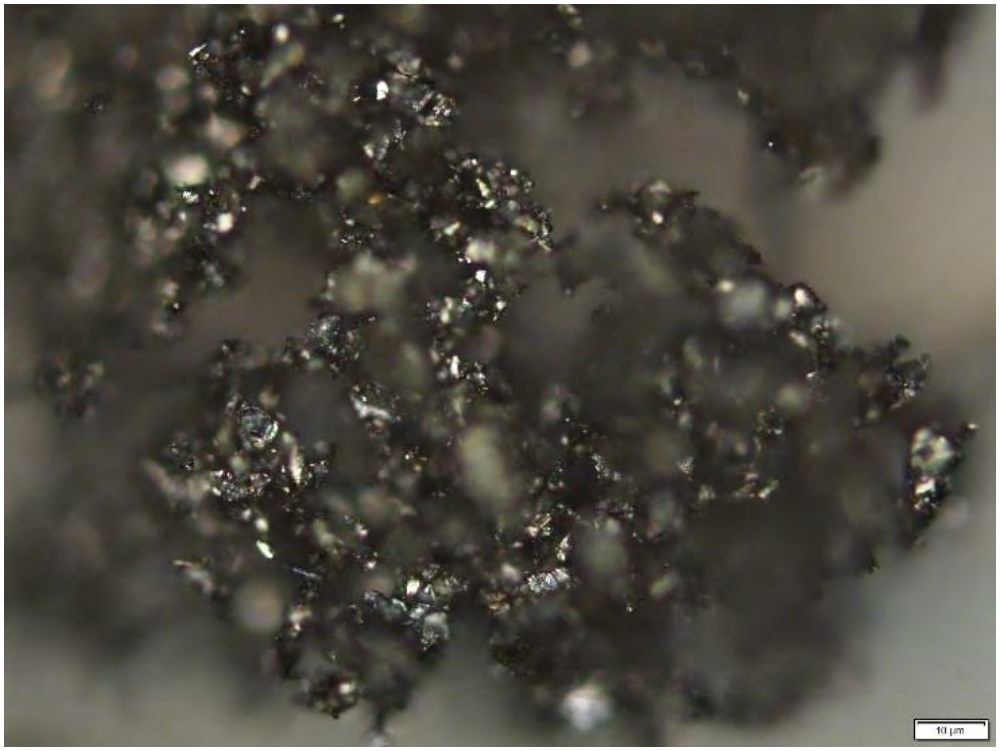

Figure S1 Photograph of the surface of bulk Ge/GeP.

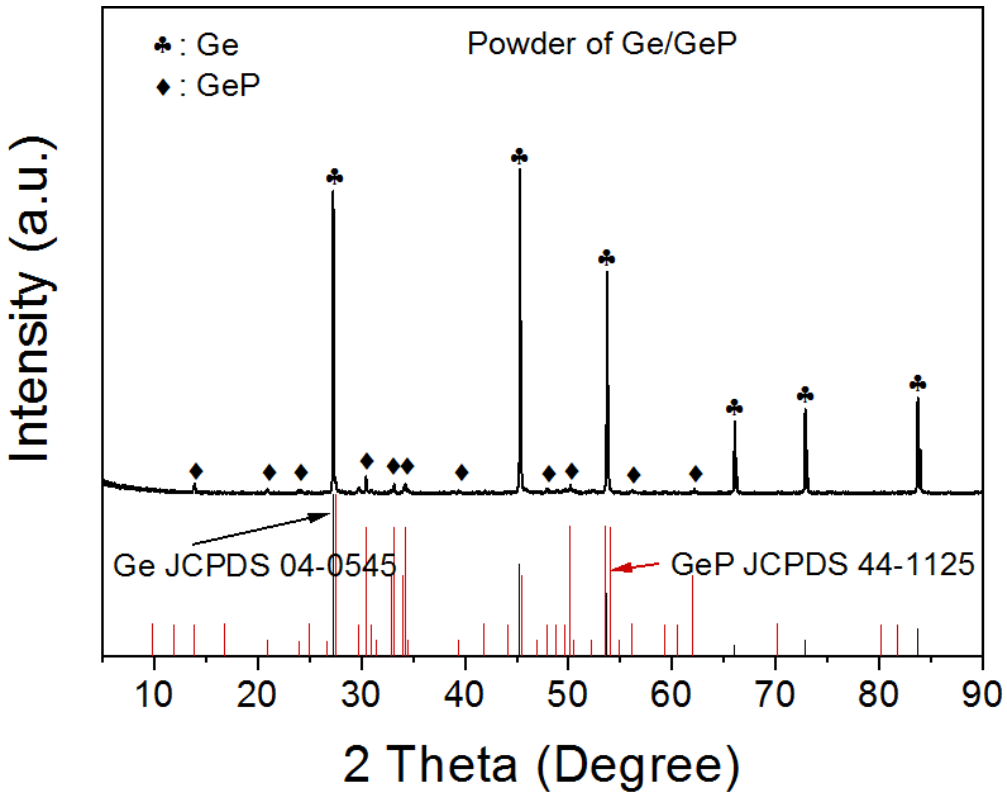

Figure S2 XRD pattern of the Ge/GeP powder.

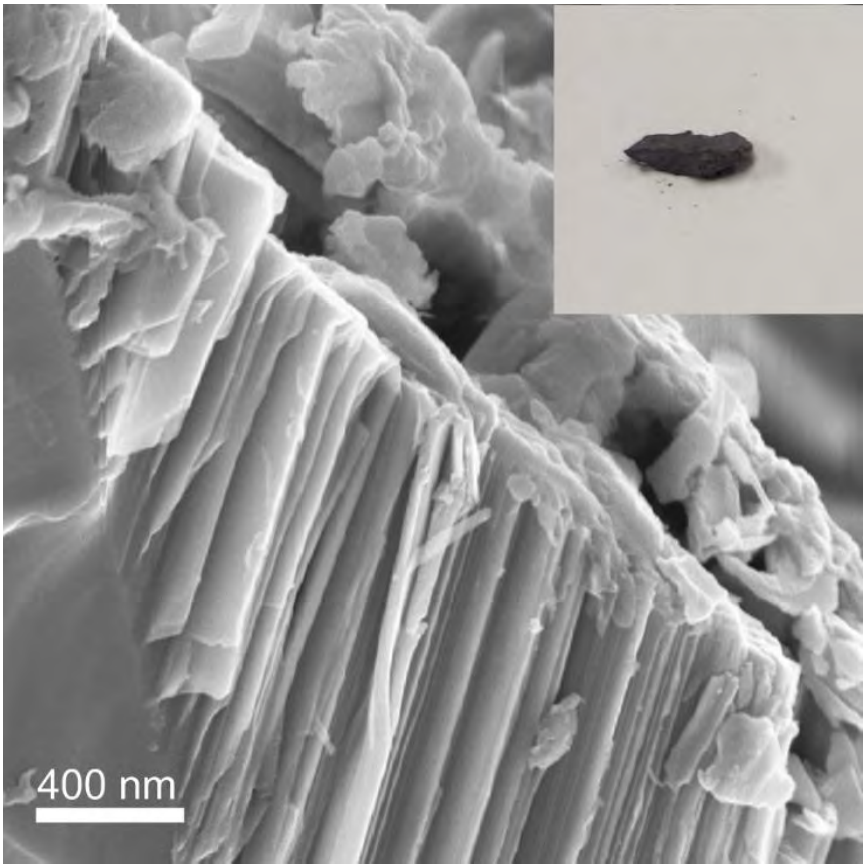

Figure S3 Intermediate product of the CVT process.

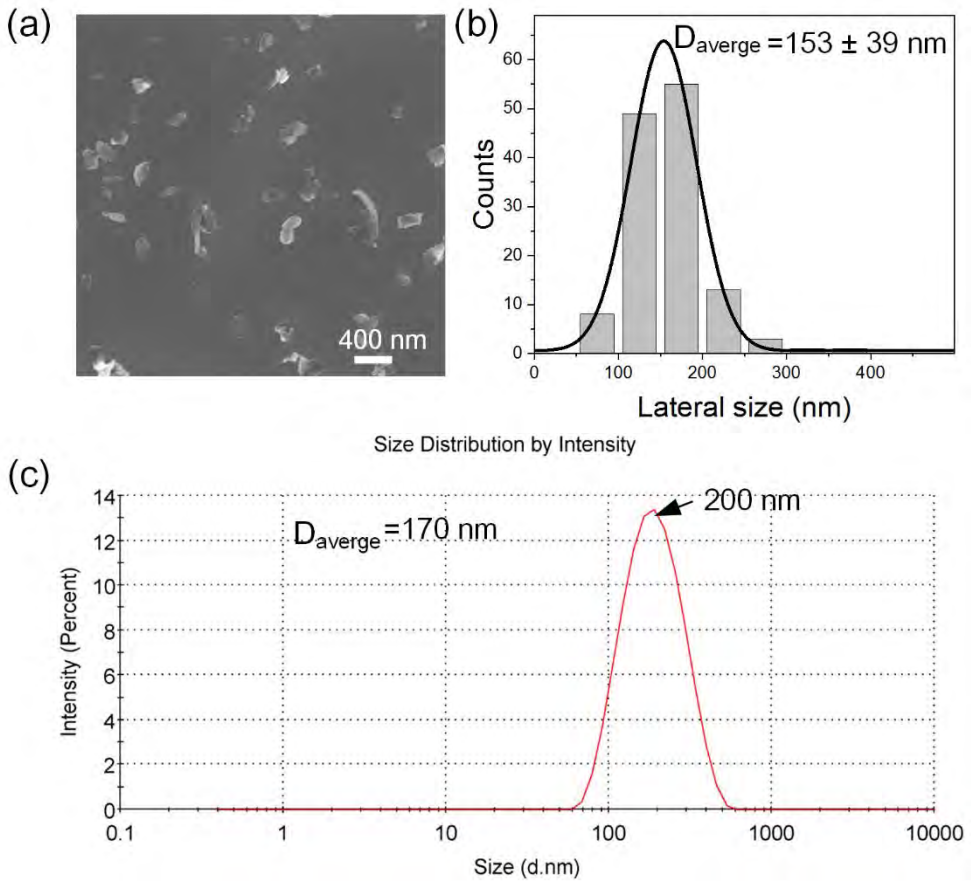

Figure S4 (a) SEM image and (b) Lateral size distribution of the Ge/GeP NSs. (c) Hydrate particle size distribution.

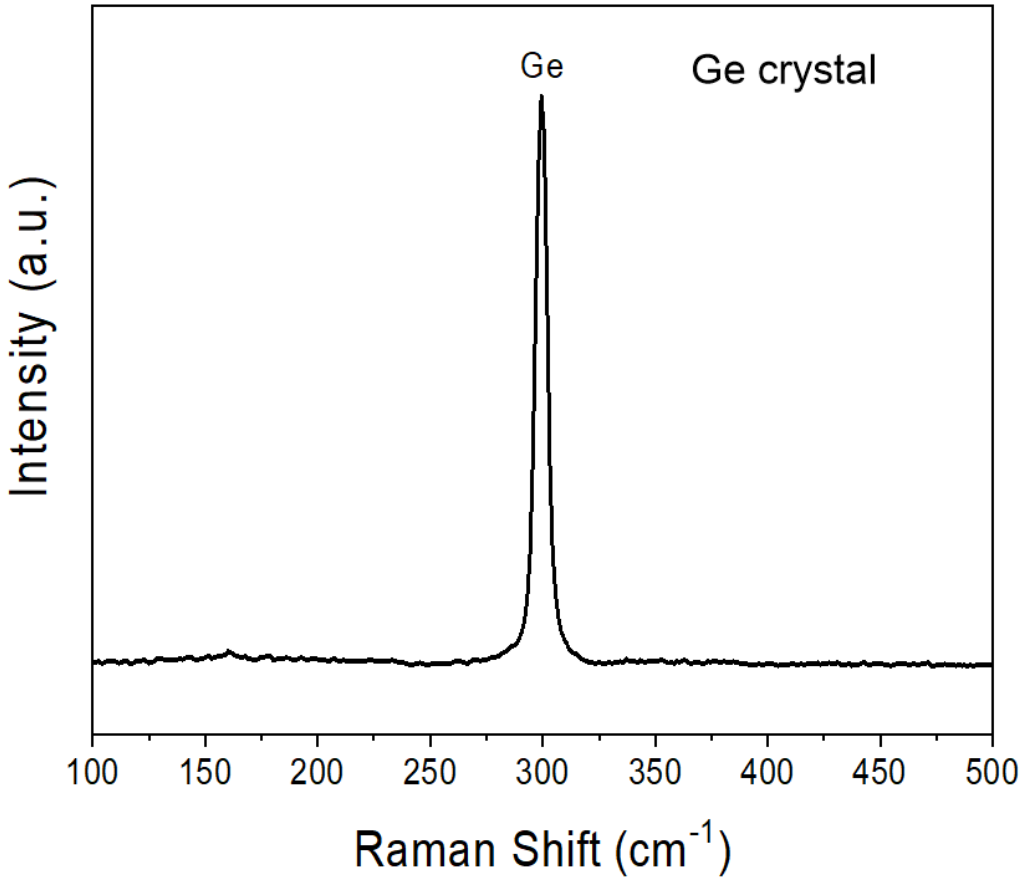

Figure S5 Raman spectrum of the Ge crystal.

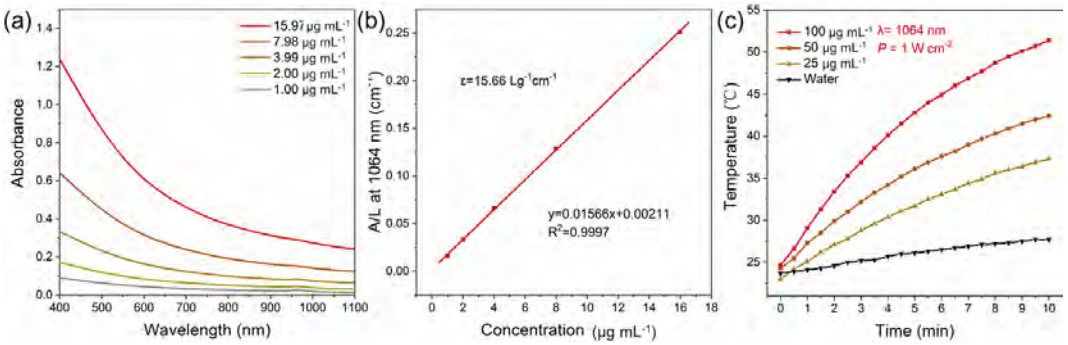

Figure S6 (a) Absorption spectra of the Ge/GeP NSs with different concentrations; (b) Corresponding linear curve of the normalized absorbance intensity divided by the optical distance (A/L) at various concentrations for λ = 1,064 nm; (c) Photothermal heating curves of the Ge/GeP NSs solutions (0, 25, 50, 100 μg mL^{-1}) under 1,064 nm NIR laser irradiation with a power of 1.0 W cm^{-2}.

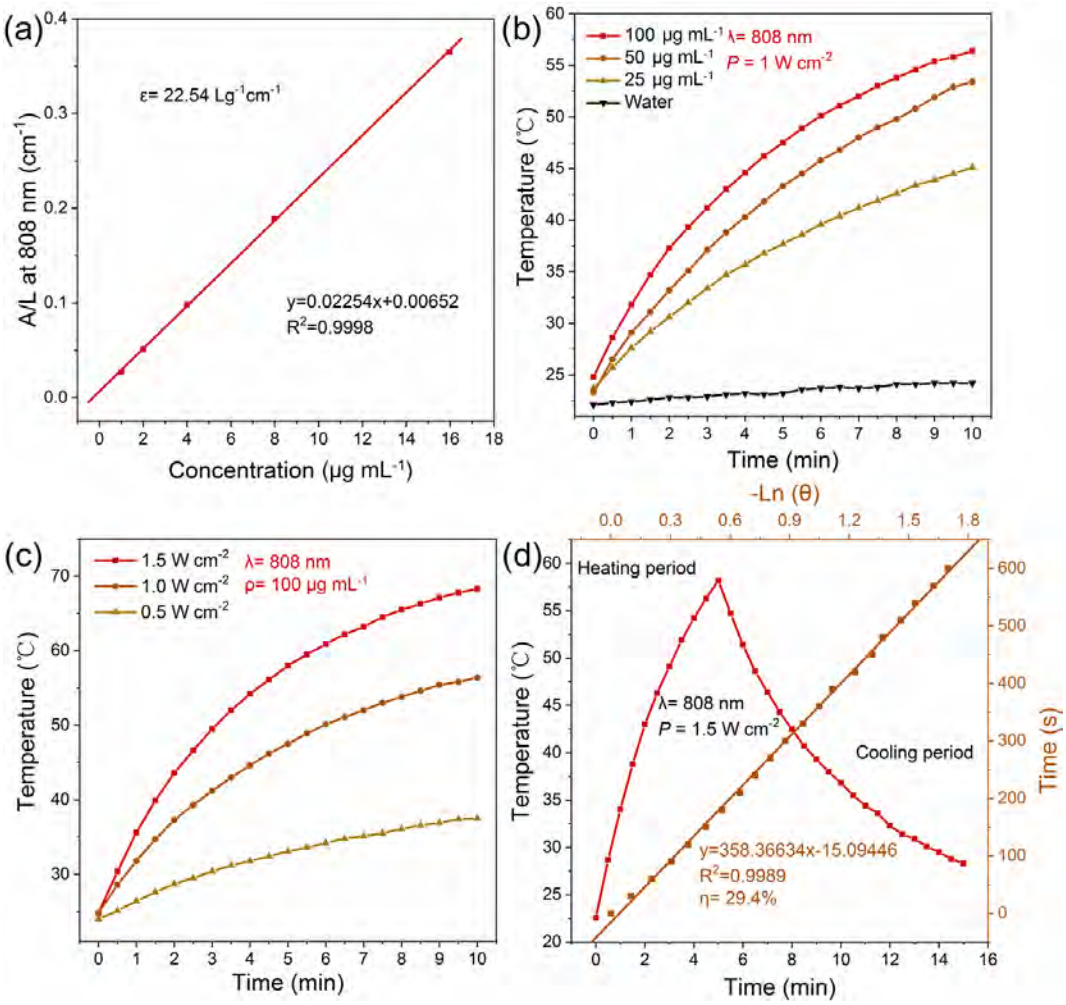

Figure S7 (a) Linear curve of the normalized absorbance intensity divided by the optical distance (A/L) at various concentrations for λ = 808 nm; (b) Photothermal heating curves of the Ge/GeP NSs solutions (0, 25, 50, and 100 μg mL^{-1}) under 808 nm NIR laser irradiation at 1.0 W cm^{-2}; (c) Photothermal heating curves of the Ge/GeP NSs solution (100 μg mL^{-1}) under 808 nm NIR laser irradiation with a power of 0.5, 1.0, or 1.5 W cm^{-2}; (d) Temperature change and photothermal-conversion efficiency under 808 nm laser irradiation.

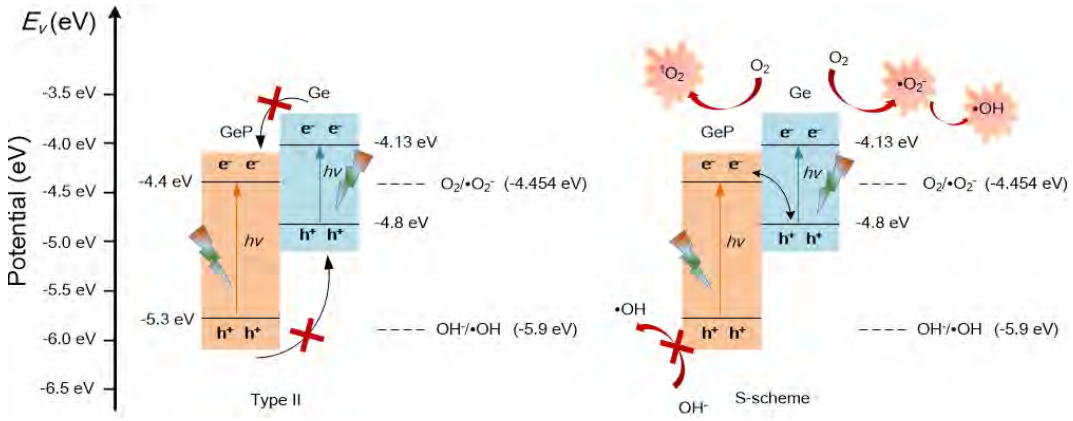

Figure S8 Band structure and ROS generating ability of the Ge/GeP NSs.

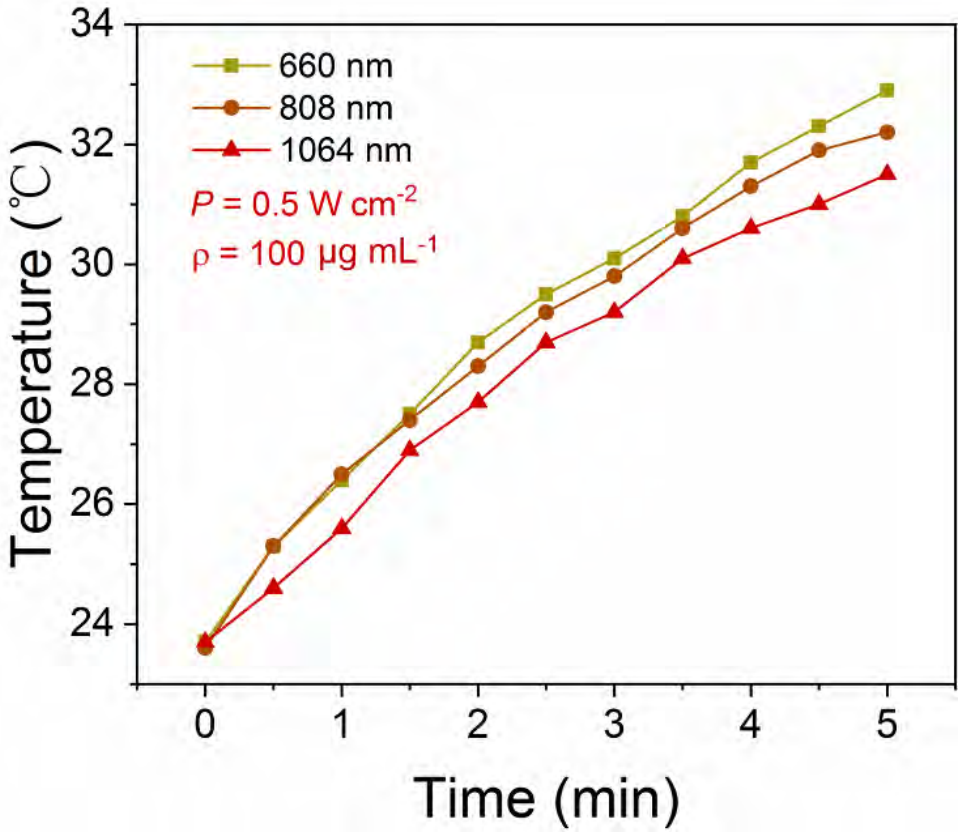

Figure S9 Photothermal heating curves of the Ge/GeP NSs solution (100 μg mL^{-1}) for different laser irradiation.

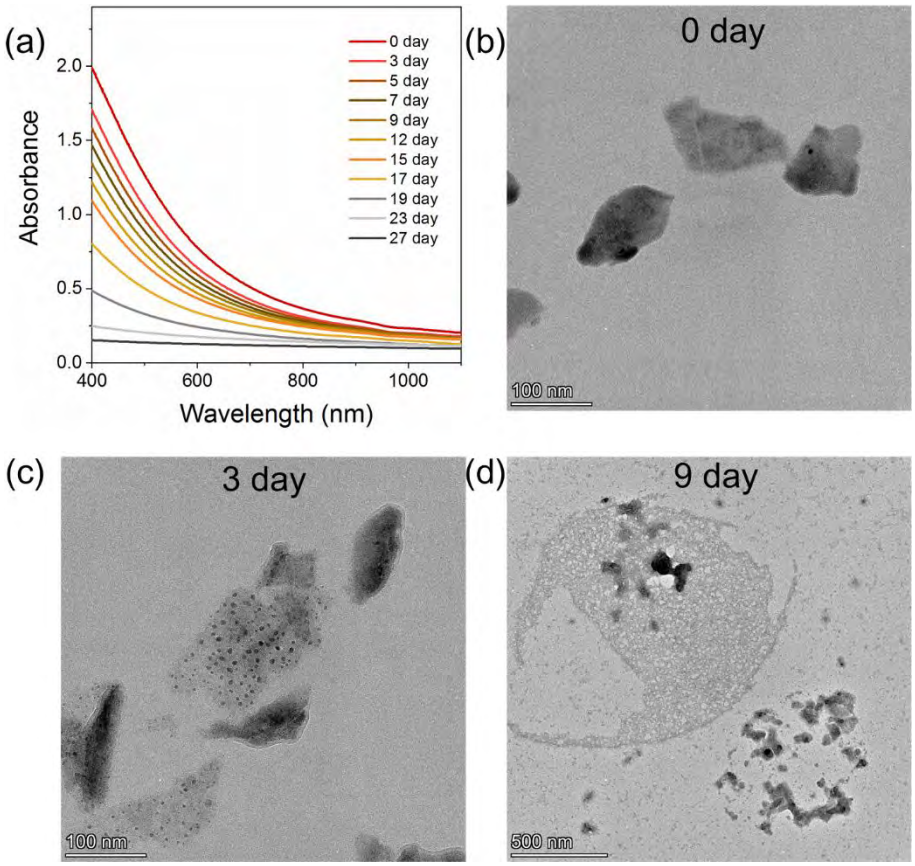

Figure S10 (a) Absorption spectra of the Ge/GeP NSs stored in water for different days and (b - d) TEM images acquired after 0, 3, and 9 days.

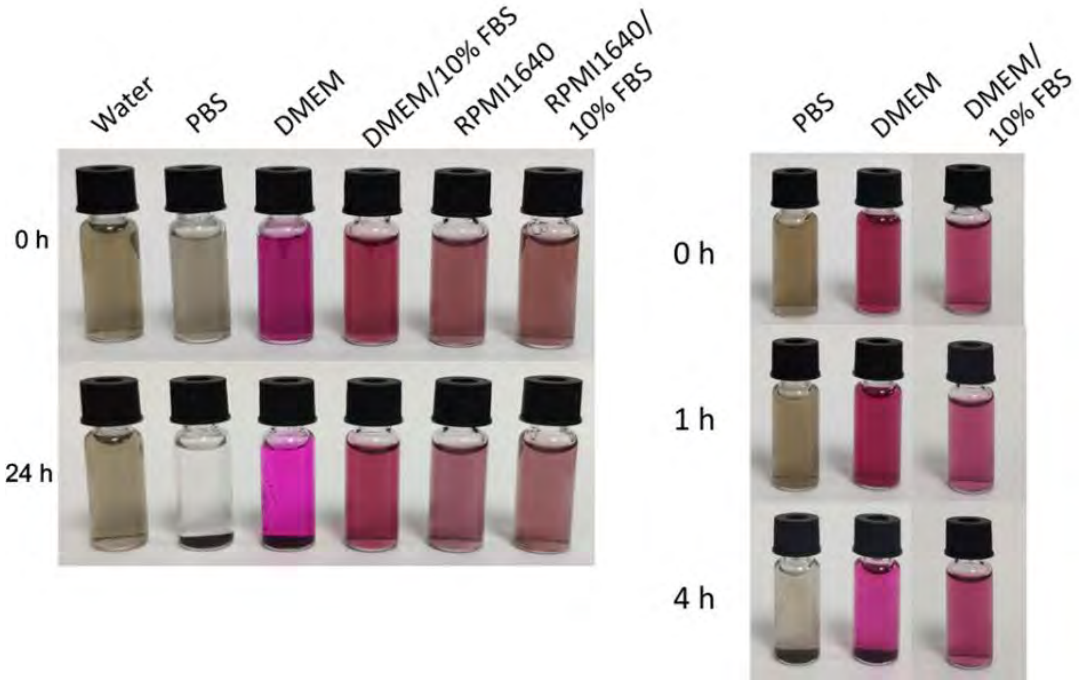

Figure S11 Dispersity of the Ge/GeP NSs in water, PBS, serum-free DMEM, DMEM/10% FBS, serum-free RPMI1640, and RPMI1640/10% FBS.

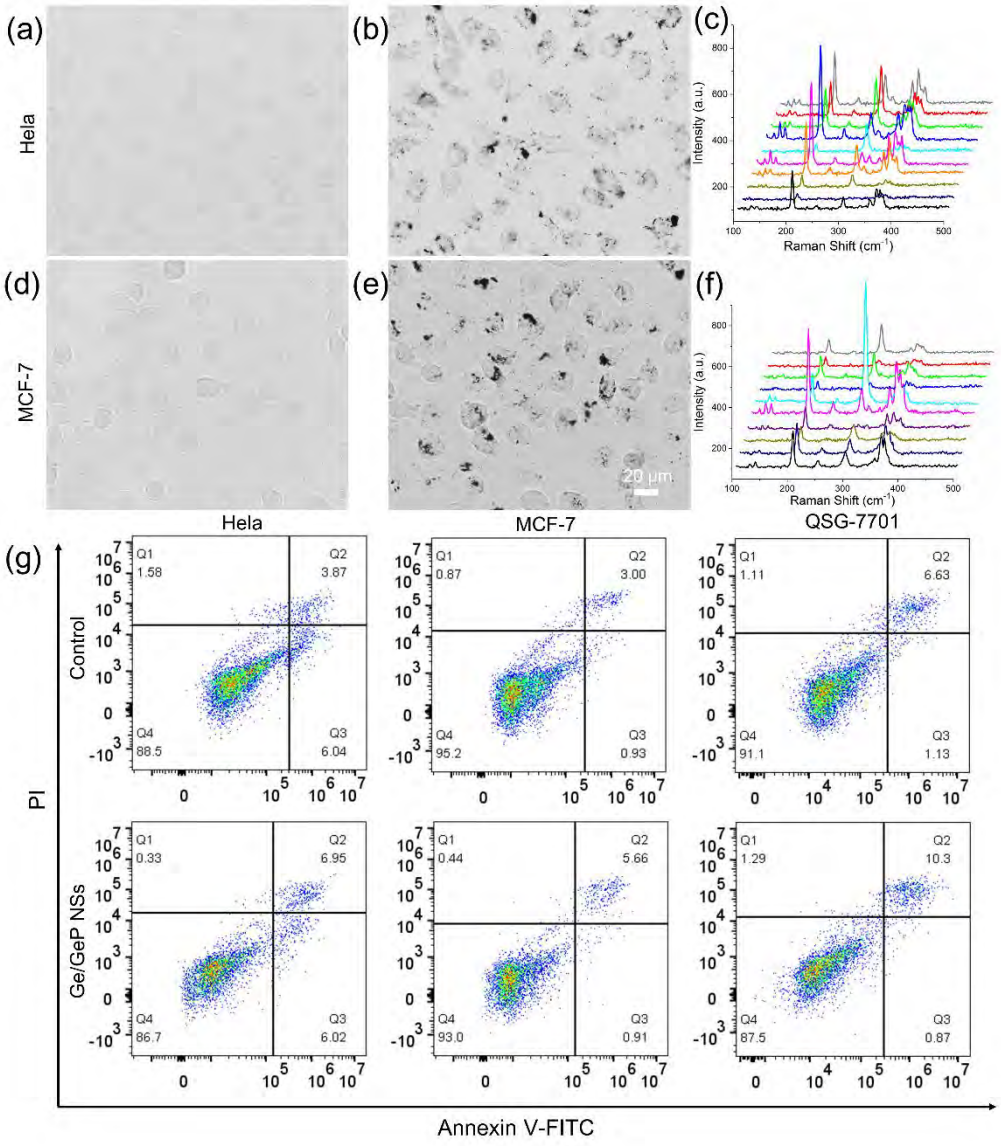

Figure S12 (a, b) Images of the Hela cells incubated without or with the Ge/GeP NSs; (c) Raman scattering spectra of the Hela cells incubated with the Ge/GeP NSs; (d, e) Images of the MCF-7 cells incubated without or with the Ge/GeP NSs; (f) Raman scattering spectra of the MCF-7 cells incubated with the Ge/GeP NSs; (g) Cell apoptosis of the Ge/GeP NSs treated Hela, MCF-7 and QSG-7701 cells measured by flow cytometry.

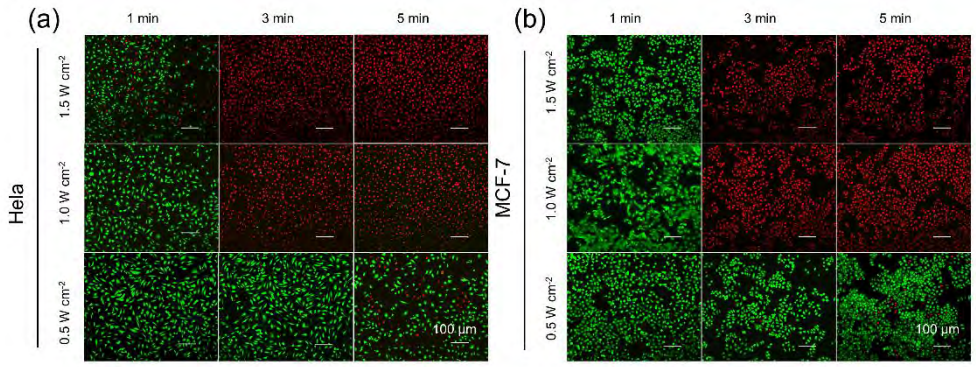

Figure S13 Fluorescence images of 100 μg mL^{-1} of the Ge/GeP NSs treated Hela and MCF-7 cells after 1,064 nm laser irradiation for different time using different power.

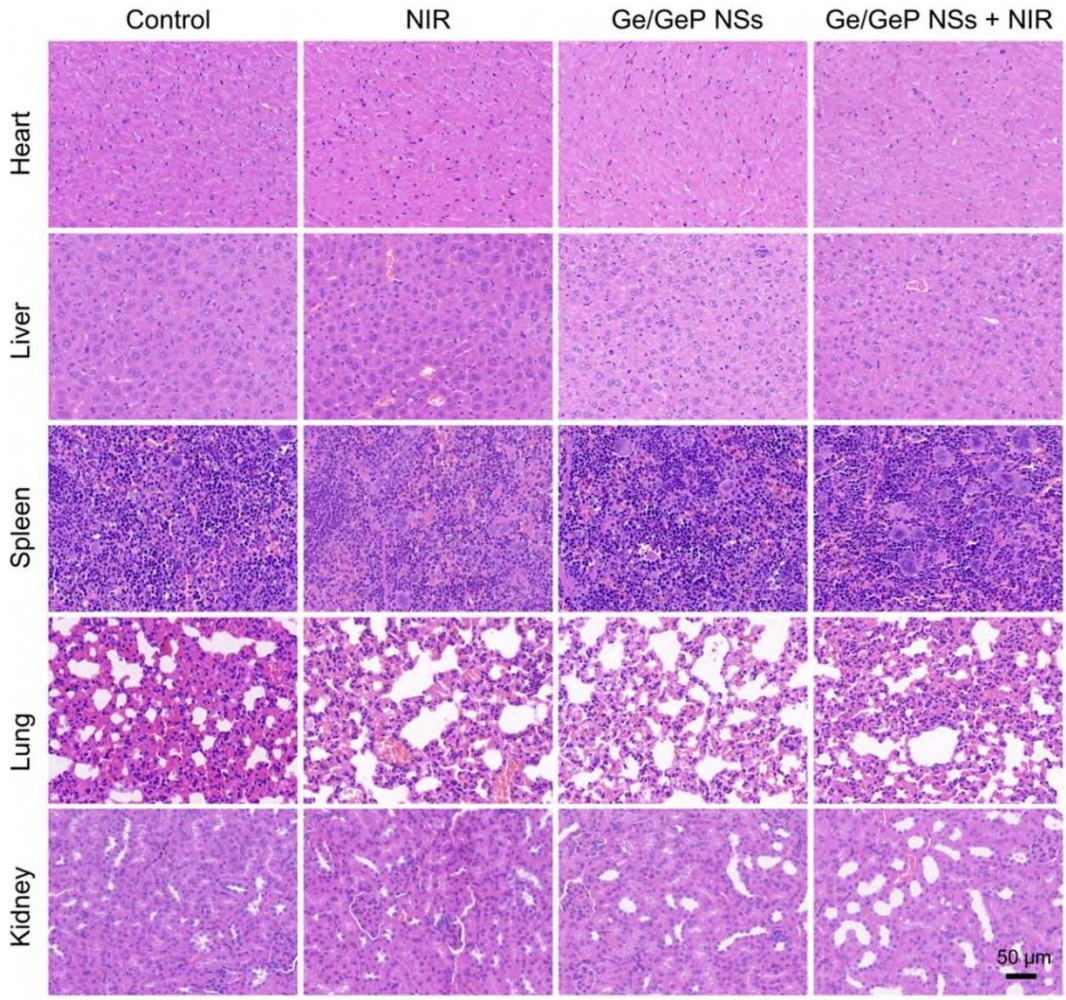

Figure S14 H&E staining of the major organs (liver, kidney, heart, lung, and spleen) for the different groups of mice on the 14th day post-intratumoral injection of Ge/GeP NSs.

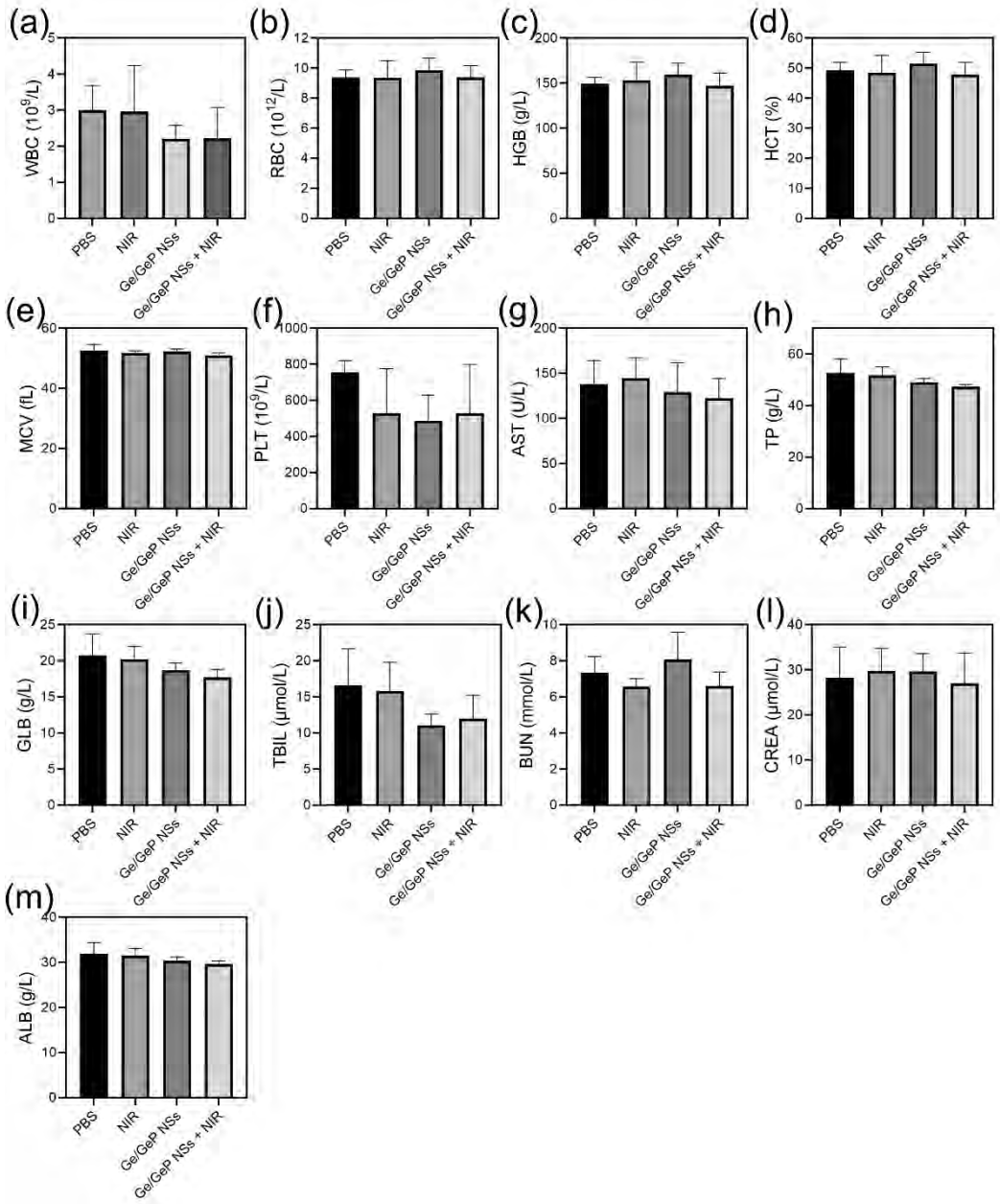

Figure S15 Hematological and blood biochemical assays of the different groups of mice on the 14th day post-intratumoral injection of Ge/GeP NSs (n = 5).

Table S1. Phototherapeutic characteristics of different nanoagents reported in the literature.

Materials	Treatment	Power density and irradiation time	References
APP/Ce6-Loaded ADSCs	PTT, PDT	1.0 W cm^{-2}, 5 min (808 nm) + 1.0 W cm^{-2}, 10 min (660 nm)	[1]
COF−CuSe	PTT, PDT	0.5 W cm^{-2}, 5 min (650 nm) + 1.5 W cm^{-2}, 5 min (808 nm)	[2]
Carbon–Silica Nanocomposite	PTT, PDT	2.0 W cm^{-2}, 3 min (808 nm)	[3]
PEG@S-MoOx A-NRs	PTT, PDT	1.0 W cm^{-2}, 10 min (808 nm)	[4]
[PHC]PP@HA NPs	PTT, PDT	1.0 W cm^{-2}, 10 min (808 nm) + 0.1 W cm^{-2}, 15 min (670 nm)	[5]
BPN/MnO_2/DOX nanocomposite	PTT, PDT, Chemotherapy	1.0 W cm^{-2}, 5 min (808 nm) + 0.22 W cm^{-2}, 10 min (660 nm)	[6]
Au/Ag NRs	PTT, PDT	1.5 W cm^{-2}, 15 min (1064 nm)	[7]
PTTe NPs	PTT, PDT	1.0 W cm^{-2}, 10 min (1064 nm),	[8]
Ce6-RCDs	PTT, PDT	0.5 W·cm^{-2}, 20 min (671 nm)	[9]
RGD-PMCS	PTT, PDT	2.0 W cm^{-2}, 3 min (808 nm)	[10]
ZnPc NPs	PTT, PDT	0.7 W cm^{-2}, 10 min (650 nm)	[11]
Bi_2Se_3@AIPH NPs	PTT, PDT	1.0 W cm^{-2}, 5 min (808 nm)	[12]
BiNS-Fe@Fe	PTT, PDT, CDT	1.31 W cm^{-2}, 5 min (808 nm)	[13]
CSNPs@Cu-BIF nanoassemblies	PTT, PDT, CDT	2.0 W cm^{-2}, 10 min (808 nm)	[14]
$CeVO_4$/Ag Nanohybrid	PTT, PDT	1.9 W cm^{-2}, 5 min (808 nm)	[15]
AuNSs@PDA-Ce6	PTT, PDT	1.0 W cm^{-2}, 5 min (808 nm) + 0.05 W cm^{-2}, 5 min (635 nm)	[16]
BNs-BSA	PTT, PDT	0.1 W cm^{-2}, 10 min (660 nm)	[17]

		+ 1.0 W cm^{-2}, 6 min (808 nm)	
Au/Pd ONP-DNA nanomachine	PTT, PDT	1.5 W cm^{-2}, 5 min (808 nm)	[18]
Bi_2Se_3/$MoSe_2$/Bi_2Se_3@PEG-Dox	PTT, PDT, chemotherapy	1.0 W cm^{-2}, 20 min (808 nm)	[19]
HA-BP nanoparticles	PTT, PDT photo-immunotherapy	0.5 W cm^{-2}, 5 min (635 nm) + 1.5 W cm^{-2}, 2 min (808 nm)	[20]

1

2

References

[1] C. C. Chuang, Y. N. Chen, Y. Y. Wang, Y. C. Huang, S. Y. Lin, R. Y. Huang, Y. Y. Jang, C. C. Yang, Y. F. Huang, C. W. Chang, *ACS Appl. Mater. Inter.* **2020**, *12*, 30021.

[2] C. Hu, Z. Zhang, S. Liu, X. Liu, M. Pang, *ACS Appl. Mater. Inter.* **2019**, *11*, 23072.

[3] H. Wang, X. Pan, X. Wang, W. Wang, Z. Huang, K. Gu, S. Liu, F. Zhang, H. Shen, Q. Yuan, J. Ma, W. Yuan, H. Liu, *ACS Nano* **2020**, *14*, 2847.

[4] Y. Wang, N. Gong, Y. Li, Q. Lu, X. Wang, J. Li, *J. Am. Chem. Soc.* **2020**, *142*, 1735.

[5] Y. Wang, S. Luo, Y. Wu, P. Tang, J. Liu, Z. Liu, S. Shen, H. Ren, D. Wu, *ACS Nano* **2020**, *14*, 17046.

[6] Q. Wu, G. Chen, K. Gong, J. Wang, X. Ge, X. Liu, S. Guo, F. Wang, *Matter* **2019**, *1*, 496.

[7] L. Jin, S. Shen, Y. Huang, D. Li, X. Yang, *Biomaterials* **2021**, *268*, 120582.

[8] K. Wen, H. Tan, Q. Peng, H. Chen, H. Ma, L. Wang, A. Peng, Q. Shi, X. Cai, H. Huang, *Adv. Mater.* **2022**, *34*, 2108146.

[9] S. Sun, J. Chen, K. Jiang, Z. Tang, Y. Wang, Z. Li, C. Liu, A. Wu, H. Lin, *ACS Appl. Mater. Inter.* **2019**, *11*, 5791.

[10] F. Zhang, Y. Liu, J. Lei, S. Wang, X. Ji, H. Liu, Q. Yang, *Adv. Sci.* **2019**, *6*, 1901378.

[11] Z. Wang, S. Gai, C. Wang, G. Yang, C. Zhong, Y. Dai, F. He, D. Yang, P. Yang, *Chem. Eng. J.* **2019**, *361*, 117.

[12] X. Li, Y. Liu, F. Fu, M. Cheng, Y. Liu, L. Yu, W. Wang, Y. Wan, Z. Yuan, *Nano-micro Lett.* **2019**, *11*, 68.

[13] S. Ma, J. Xie, L. Wang, Z. Zhou, X. Luo, J. Yan, G. Ran, *ACS Appl. Mater. Inter.* **2021**, *13*, 10728.

[14] Y. Qi, J. Ye, S. Ren, G. Wang, J. Lv, S. Zhang, Y. Che, Y. Li, B. Chen, G. Ning, *Adv. Healthc. Mater.* **2020**, *9*, 2001205.

[15] M. Chang, M. Wang, Y. Chen, M. Shu, Y. Zhao, B. Ding, Z. Hou, J. Lin, *Nanoscale* **2019**, *11*, 10129.

[16] Z. Li, F. Yang, D. Wu, Y. Liu, Y. Gao, H. Lian, H. Zhang, Z. Yin, A. Wu, L. Zeng, *Nanoscale* **2020**, *12*, 22173.

[17] Y. Wang, W. Feng, M. Chang, J. Yang, Y. Guo, L. Ding, L. Yu, H. Huang, Y. Chen, J. Shi, *Adv. Funct. Mater.* **2020**, *31*, 2005093.

[18] Z. Cai, Y. Fu, Z. Qiu, Y. Wang, W. Wang, W. Gu, Z. Li, S. Wu, F. Gao, *ACS Nano* **2021**, *15*, 19150.

[19] Y. Wang, J. Zhao, Z. Chen, F. Zhang, Q. Wang, W. Guo, K. Wang, H. Lin, F. Qu, *Biomaterials* **2019**, *217*, 119282.

[20] X. Zhang, J. Tang, C. Li, Y. Lu, L. Cheng, J. Liu, *Bioact. Mater.* **2021**, *6*, 472.